1   **Cell lineage as a predictor of immune response in neuroblastoma**

2

3   Satyaki Sengupta[1,2,*], Sanjukta Das[1,2,*], Angela Crespo[2,3], Brian Miller[4,5,6,7], Bandana Sharma[1,2],

4   Shupei Zhang[8], Ruben Dries[1,2], Hao Huang[1,2], Malgorzata Krajewska[1,2], David N. Debruyne[1,2],

5   Luigi Soriano[1], Malkiel A. Cohen[8], Rogier Versteeg[9], Rudolf Jaenisch[8,10], Stefani Spranger[10,11],

6   Judy Lieberman[2,3], Rani E. George[1,2,12]

7

8   [1]Department of Pediatric Oncology, Dana-Farber Cancer Institute, Boston, MA 02215, USA

9   [2]Department of Pediatrics, Harvard Medical School, Boston, MA 02215, USA

10   [3]Program in Cellular and Molecular Medicine, Boston Children's Hospital, Boston, MA, USA.

11   [4]Broad Institute of MIT and Harvard, Cambridge, Massachusetts 02142, USA.

12   [5]Department of Medical Oncology, Dana-Farber Cancer Institute and Harvard Medical School,

13   Boston, Massachusetts 02215 USA.

14   [6]Department of Immunology, Blavatnik Institute, Harvard Medical School, Boston, MA, USA

15   [7]Evergrande Center for Immunological Diseases, Harvard Medical School and Brigham and

16   Women's Hospital, Boston, MA, USA.

17   [8]Whitehead Institute for Biomedical Research, 455 Main Street, Cambridge, MA 02142, USA

18   [9]Department of Oncogenomics, Amsterdam UMC University of Amsterdam, Meibergdreef 9,

19   1105 AZ Amsterdam, The Netherlands

20   [10]Department of Biology, Massachusetts Institute of Technology, Cambridge, MA 02142,

21   USA

22   [11]Koch Institute for Integrative Cancer Research, Cambridge, MA 02142, USA

23   *These authors contributed equally

24   [12]Corresponding author: rani_george@dfci.harvard.edu

25

26

27 **SUMMARY**

28 Immunotherapy for patients with neuroblastoma has met with limited success, partly due to an

29 incomplete understanding of the mechanisms underlying immune responsiveness in this clinically

30 and genetically heterogenic tumor. Here, we undertook an unbiased analysis using dimension

31 reduction and UMAP visualization of transcriptional signatures derived from 498 primary

32 neuroblastoma tumors. Four distinct clusters based on differentially expressed genes emerged,

33 of which one, representing about 30% and comprising mainly of *MYCN*-nonamplified tumors, was

34 notable for the high expression of genes associated with both immune response activation and

35 suppression. This capacity to elicit a productive immune response resided exclusively in tumors

36 with dominant populations of undifferentiated, neural crest-like or mesenchymal cells; by contrast,

37 tumors comprising primarily of committed, adrenergic neuron-like cells were less immunogenic.

38 Mesenchymal neuroblastoma cells were enriched for innate and adaptive immune gene

39 signatures, demonstrated engagement with cytotoxic T and natural killer cells, and induced

40 immune cell infiltration in an immunocompetent mouse model. Transcriptional or targeted therapy-

41 induced reprogramming of adrenergic cells to the mesenchymal state led to reactivation of tumor

42 cell-intrinsic immune genes. Key immune response genes in adrenergic tumor cells were found

43 to be epigenetically silenced by the PRC2 complex, and such repression could be relieved by

44 either mesenchymal cell state reprogramming or EZH2 inhibition, leading to increased activation

45 of natural killer cells by the tumor cells. These data identify cell lineage as a major determinant of

46 the immunogenic potential in neuroblastoma that could be used to stratify patients who are most

47 likely to benefit from immunotherapy.

48 **INTRODUCTION**

49 The anti-disialoganglioside GD2 monoclonal antibody dinutuximab has significantly improved

50 event free survival rates in neuroblastoma[1]. Derived from the developing neural crest, this

51 common solid tumor of childhood manifests as an extracranial mass arising in the adrenal medulla

52 or sympathetic ganglia. Approximately half of all patients have high-risk features associated with

53 a poor outcome - age >18 months, distant metastases and unfavorable histologic and genetic

54 factors including amplification of the *MYCN* oncogene[2]. The success of anti-GD2 therapy that

55 relies on immune cell-mediated cytotoxicity suggests that patients with neuroblastoma would

56 benefit from other forms of immunotherapy; however, treatment results with use of cytotoxic CD8+

57 T lymphocytes directed against neuroblastoma antigens[3], adoptive transfer of chimeric antigen

58 receptor (CAR)-modified T cells[4-6] or checkpoint inhibition[7,8] have been suboptimal.

59

60 Major impediments to the effectiveness of immunotherapy in neuroblastoma are the immune

61 evasion tactics deployed by the tumor cells as well as the tumor microenvironment (TME)[9]. These

62 include downregulation of major histocompatibility complex (MHC) class I molecules and defects

63 in antigen-processing machinery (APM) that render neuroblastoma cells resistant to T-cell-

64 mediated cytotoxicity[10-12], downregulation of cell-surface ligands required for natural killer (NK)

65 cell receptor activation[13], upregulation of checkpoint proteins that exert a protective role from NK

66 cell-mediated lysis[14], inefficient homing of cytotoxic T-cells to the tumor site[15] or tumor cell

67 overexpression of the leukocyte surface antigen CD47, which enables avoidance of macrophage-

68 mediated phagocytosis[16]. Moreover, infiltration of suppressive immune cells such as T regulatory

69 cells[17], tumor-associated macrophages (TAMs)[18,19], myeloid-derived suppressor cells[20] and

70 secreted immunosuppressive factors such as TGF-β, contribute to the generation of a TME that

71 hinders an effective immune response and further dampens the effects of adoptive cell

72 therapies[21].

73

74   Amplification of the MYCN oncogene poses another distinct challenge to immunotherapy in

75   neuroblastoma. This transcription factor is amplified in approximately 50% of high-risk cases and

76   is associated with aggressive disease and a poor clinical outcome[22,23]. *MYCN*-amplified tumors

77   consistently evade immune destruction by downregulating MHC class I molecules[10] and are

78   associated with poor infiltration of cytotoxic CD8^{+} T cells[24,25] and reduced expression of NK cell

79   ligands[26]. Interestingly, approximately half of high-risk neuroblastomas do not express amplified

80   *MYCN*, and their capacity to induce a productive immune response remains unclear. In a recent

81   study that analyzed the immune gene expression programs associated with *MYCN*-nonamplified

82   tumors from high-risk patients, tumors with low as well as high functional tumor *MYCN* signatures

83   were observed to have significantly higher levels of NK and CD8+ T-cell infiltrates compared to

84   *MYCN*-amplified tumors; although, somewhat counterintuitively, these findings translated into a

85   better outcome only in patients with high *MYCN* tumor signatures[25,27].

86

87   Thus, although many of the mechanisms of immune evasion in neuroblastoma are known,

88   further understanding of the tumor-host interaction will be crucial to enhancing the ability of

89   immunotherapy to target and eliminate tumor-initiating and propagating cell populations.

90   Especially challenging is the genetic and biologic heterogeneity of this tumor which makes it

91   difficult to identify factors that consistently indicate the likelihood of an effective immune response

92   and hence identify patients who are most likely to benefit from this form of therapy. Thus, we

93   undertook an unbiased analysis of gene expression signatures across diverse clinical subtypes

94   of primary tumors and identify tumor cell state as an important predictor of immune

95   responsiveness in neuroblastoma.

96

97 **RESULTS**

98 **A subset of primary neuroblastomas express markers of a productive immune response**

99 To determine whether neuroblastomas are capable of eliciting a productive immune response,

100 we first examined bulk RNA-sequencing data from 498 well-annotated primary human tumors

101 representing diverse clinical and genetic subtypes (SEQC-498; GSE49711; **Supplementary Fig.**

102 **1a**) to quantify tumor-to-tumor gene expression variability and cluster tumor types based on gene

103 expression profiles (see also Methods). In this unbiased analysis, all tumors within one cluster

104 would share similar gene expression profiles, while being dissimilar to those of tumors within other

105 clusters. Specifically, we first identified the top 5000 highly variably expressed genes within this

106 dataset based on the premise that these would be most likely to contribute to distinct molecular

107 subtypes[28,29] (**Supplementary Fig. 1b; Supplementary Table 1)**. The data were dimensionally

108 reduced using principal component analysis (PCA) and the top 20 leading principal components

109 selected for clustering analysis **(Supplementary Fig. 1c)**. Four distinct clusters were identified

110 and visualized using 2D-Uniform Manifold Approximation and Projection (UMAP), a non-linear

111 dimension-reduction tool[30,31] (**Fig. 1a**). To explore the transcriptional differences between the

112 clusters, we identified the differentially expressed genes (DEGs) in each cluster and noted that

113 tumors in cluster 1 (C1; n = 103), termed *Hi-MYCN,* were enriched for MYCN target genes

114 involved in cell proliferation and biosynthesis, and comprised 20% of the tumor set (**Fig. 1a-c;**

115 **Supplementary Fig. 1d; Supplementary Table 2)**. Not surprisingly, this cluster segregated with

116 *MYCN*-amplified tumors in patients aged ≥ 18 months with stage 4 disease [according to the

117 international neuroblastoma staging system (INSS)][32] and annotated "high risk" status (based on

118 the Children's Oncology Group risk classification)[33] (**Fig. 1d; Supplementary Fig. 1e)**. The

119 remaining clusters consisted of *MYCN*-nonamplified tumors (**Fig. 1a**) of which, cluster 2 (C2, n =

120 241), or *neuronal*, made up the largest proportion of tumors, 48%, and comprised tumors that

121 were enriched for DEGs with roles in nervous system
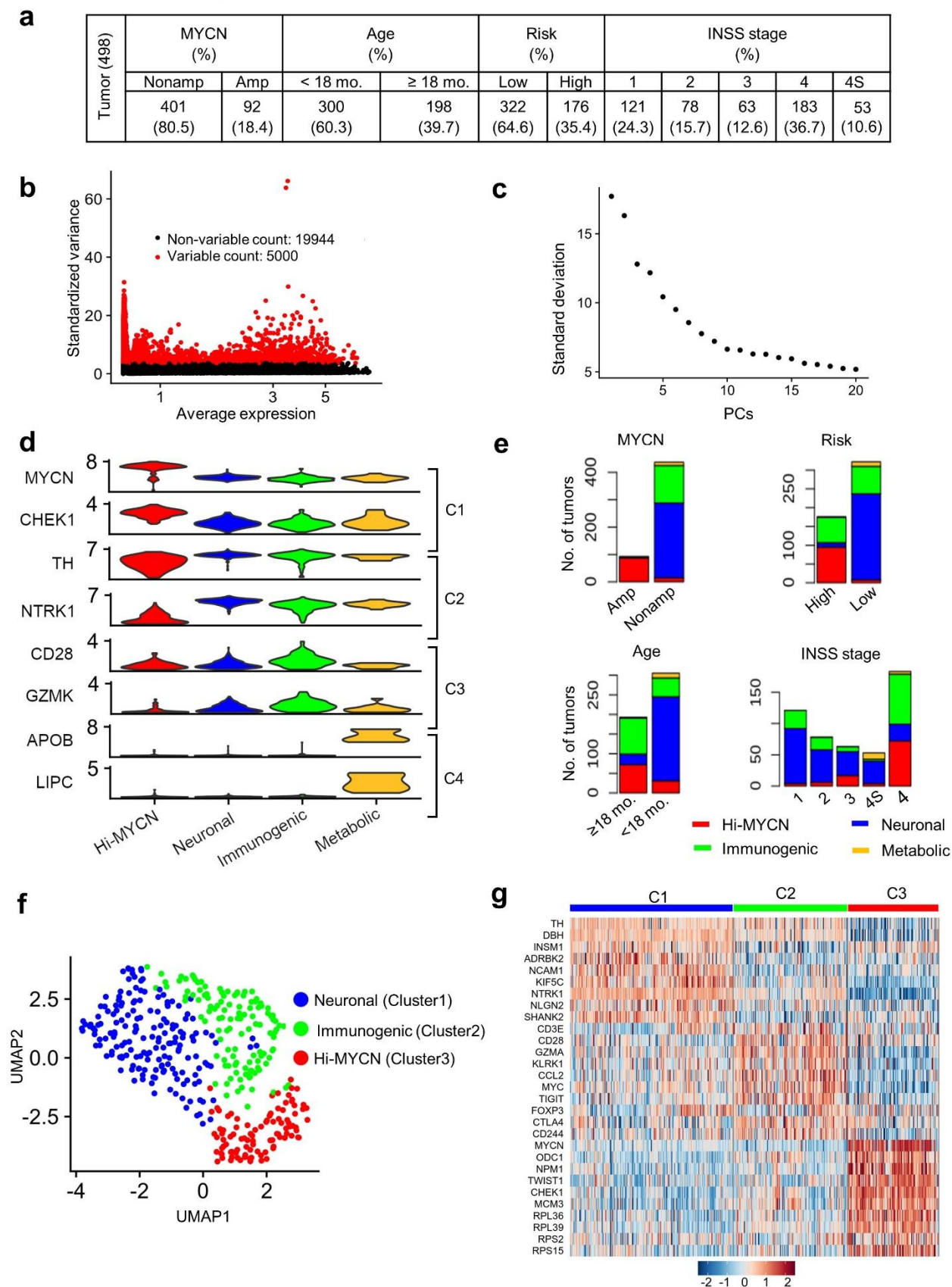
Fig. 1.
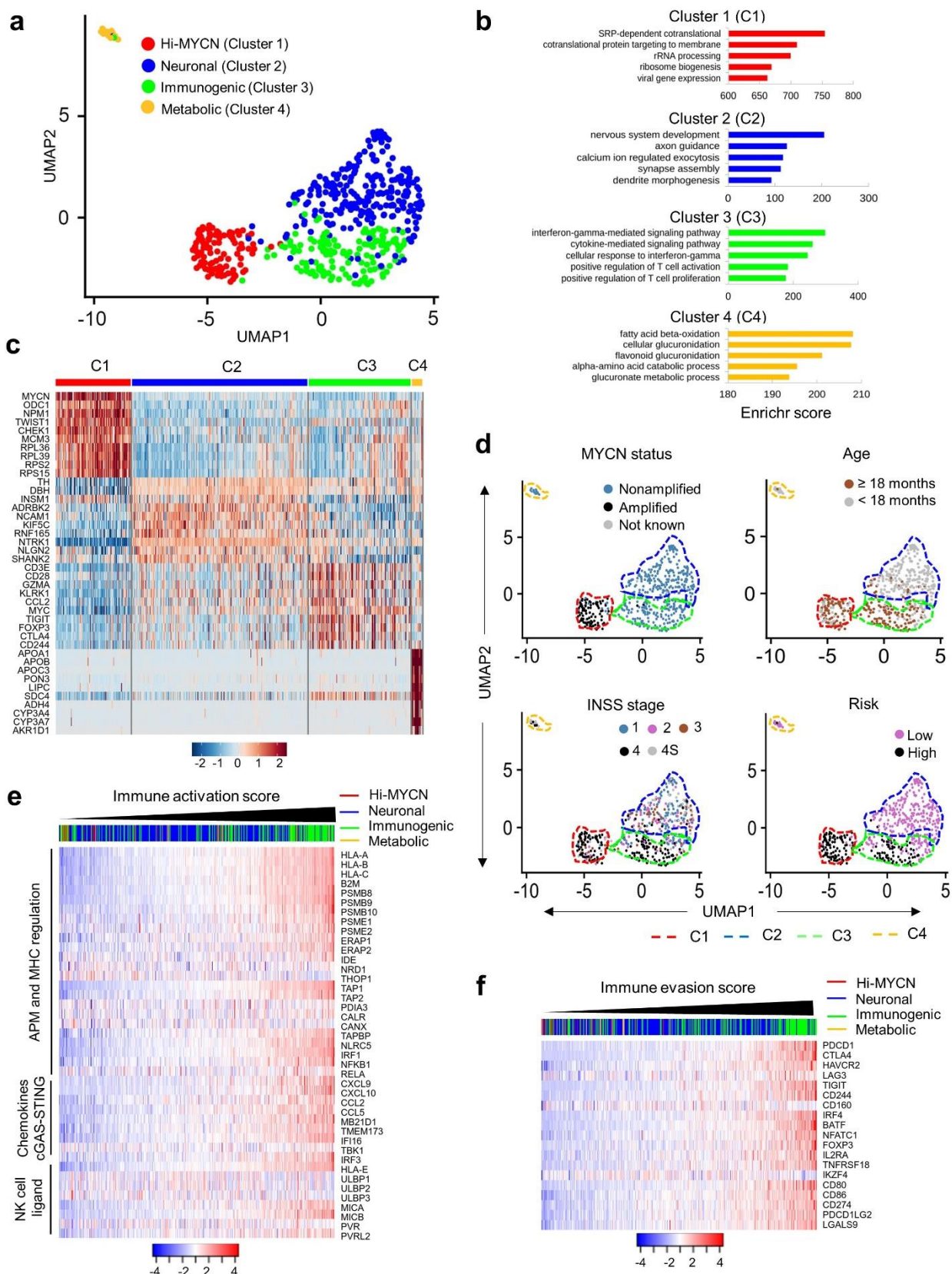
122 **Fig. 1. A subset of neuroblastomas exhibits a productive immune response. (a)** Two-

123 dimensional UMAP representations of the gene expression profiles in 498 neuroblastoma (NB)

124 tumors. Each dot represents a tumor. The top 5000 highly variable genes were selected based

125 on the variance-stabilizing method[34] and the 20 significant principal components (PCs) selected

126 and processed in UMAP to generate four clusters representing four NB subtypes. The DEGs were

127 identified for each cluster using the receiver operating characteristics (ROC) curve to compare

128 one cluster with other three (log$_2$ FC > 0.25). **(b)** Gene ontology (GO) analysis of top DEGs in the

129 four clusters. **(c)** Heat map of expression values of 10 representative DEGs within each cluster.

130 Rows are z-score scaled average expression levels for each gene in all four clusters. **(d)** UMAP

131 visualization of the distribution of the indicated prognostic features in NB among the four different

132 clusters. **(e, f)** Heat map of z-score transformed log$_2$ normalized expression values of immune

133 activation **(e)** and evasion **(f)** genes in *MYCN*-nonamplified NBs (n=401). Tumors were ranked

134 based on increasing immune activation or evasion scores**.** Cluster annotations of the tumors are

135 indicated on the top horizontal bar.

Supplementary Fig. 1.

a

|	MYCN (%)		Age (%)		Risk (%)		INSS stage (%)				
	Nonamp	Amp	< 18 mo.	≥ 18 mo.	Low	High	1	2	3	4	4S
Tumor (498)	401 (80.5)	92 (18.4)	300 (60.3)	198 (39.7)	322 (64.6)	176 (35.4)	121 (24.3)	78 (15.7)	63 (12.6)	183 (36.7)	53 (10.6)

136 **Supplementary Fig. 1. Tumors within the immunogenic cluster express both immune**

137 **activation and evasion markers. (a)** Distribution of the 498 primary NB tumors in the data set

138 (SEQC-498; GSE49711) within the indicated prognostic categories. **(b)** Scatter plot of the

139 standardized variance in expression of all protein coding genes within 498 tumors. Red dots

140 indicate the top 5000 variably expressed genes. **(c)** Elbow plot representing the percentage

141 variance for the top 20 principal components, PCs. **(d)** Violin plots showing the expression of

142 representative marker genes across the four clusters. **(e)** Stacked bar plots showing the

143 distribution of tumors within the defined prognostic features within each cluster. Amp, amplified;

144 Nonamp, nonamplified. **(f)** Two-dimensional UMAP representations of the gene expression

145 profiles in 394 NB tumors (GSE120572). Each dot represents a tumor. The top 3000 highly

146 variable genes were selected based on the variance-stabilizing method [34] and the 20 significant

147 principal components (PCs) selected and processed in UMAP to generate three clusters

148 representing three NB subtypes. The DEGs were identified for each cluster using the receiver

149 operating characteristics (ROC) curve to compare one cluster with other two ($\log_2$ FC > 0.25). **(g)**

150 Heat map of expression values of 10 representative DEGs within each cluster. Rows are z-score

151 scaled average expression levels for each gene in all three clusters.

152

Supplementary Fig. 2.

a

b

c
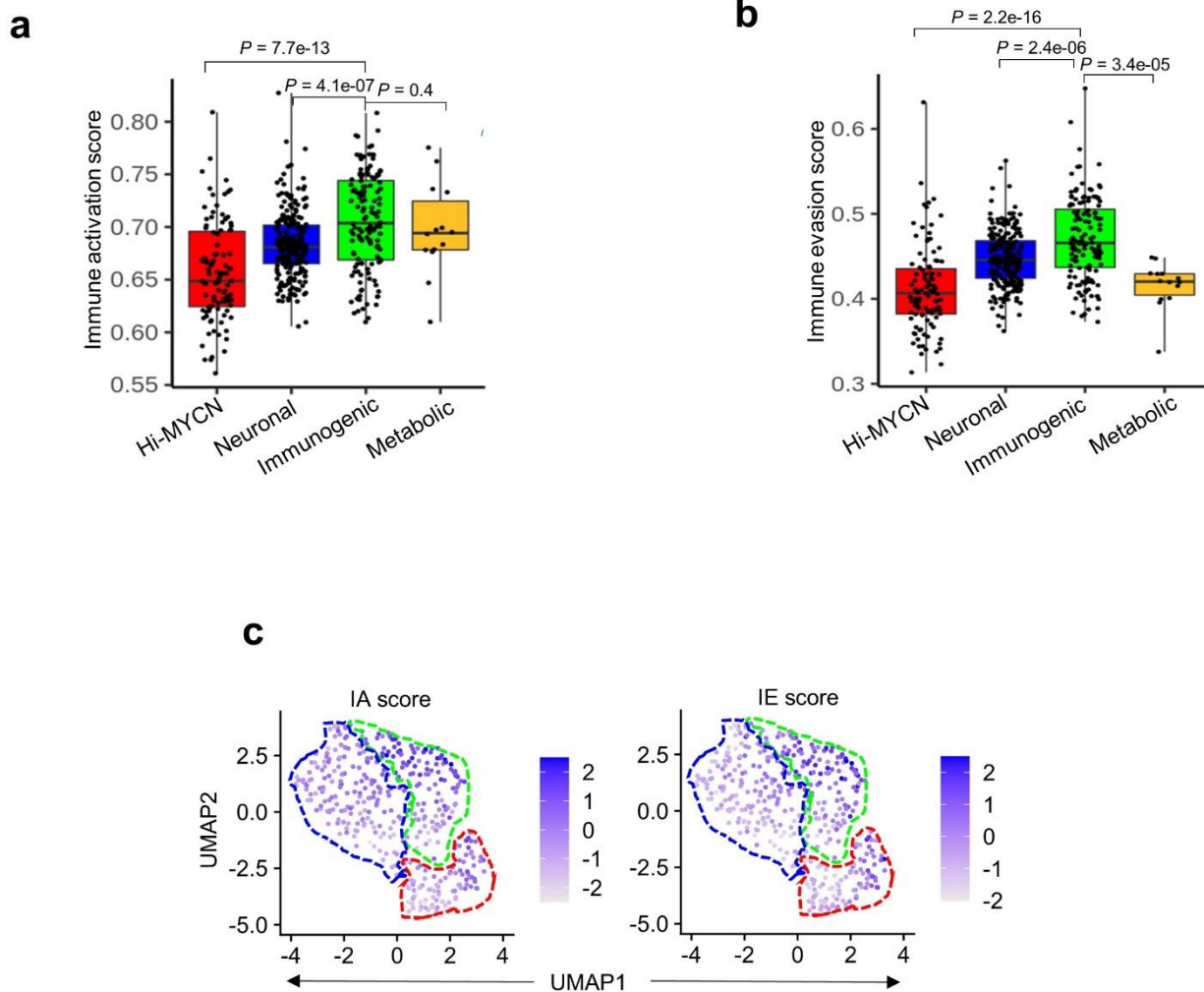
153   **Supplementary Fig. 2. The immunogenic tumors are associated with markers of both**

154   **immune activation and evasion. (a, b)** Box plots comparing immune activation **(a)** and evasion

155   **(b)** scores within the four clusters from the SEQC-498 tumor data set. All box plots are defined

156   by center lines (medians), box limits (25th and 75th percentiles), whiskers (minima and maxima;

157   the smallest and largest data range). Significance was determined by the Wilcoxon rank-sum test.

158   **(c)** UMAP visualization of the distribution of IA and IE scores among the three tumor clusters

159   derived from the 394 NBs in the GSE120572 dataset. Color bar represents normalized z-scores.

160   Values <2.5 and >2.5 were set to -2.5 and +2.5 respectively, to reduce the effects of extreme

161   outliers.

162

163 development **Fig. 1a-c; Supplementary Fig. 1d).** Cluster 3 (C3, n = 140), accounting for 28%

164 of the tumors, was enriched for tumors whose DEGs were involved in immune function, such as

165 interferon-gamma (IFN-γ) response and T cell inflammation and activation, and hence were

166 designated *immunogenic* **(Fig. 1a-c; Supplementary Fig. 1d)** . Cluster 4 (C4; n=14; 3%) was

167 clearly distinct from the other three clusters, and largely consisted of the spontaneously

168 regressing stage 4S tumors that were predominantly enriched for genes involved in fatty acid and

169 cholesterol homeostasis and hence were termed *metabolic* **(Fig. 1a-c; Supplementary Fig. 1d)**.

170 The neuronal and metabolic tumors arose predominantly in children <18 months of age, were of

171 stages 1-3 and 4S, while the tumors within the immunogenic cluster were associated with patient

172 age ≥18 months and metastatic disease (n= 66; 47%) **(Fig. 1d; Supplementary Fig. 1e)**. Thus,

173 our DEG-based analysis of almost 500 tumors categorized neuroblastoma into four largely distinct

174 groups that included a distinct subset, accounting for approximately one-third of the entire cohort,

175 whose gene expression profiles were closely linked to immune responsiveness. To ensure that

176 these results were not confined to one data set, we analyzed an independent data set of 394

177 tumors (GSE120572) using similar clustering methods. This cohort also segregated into *Hi-*

178 *MYCN, neuronal* and *immunogenic* clusters, again denoting the presence of immune response

179 gene expression in a subset of primary neuroblastomas, the majority of which lack MYCN

180 amplification **(Supplementary Fig. 1f, g)**.

181

182 To pursue the immune genes that were differentially enriched in the immunogenic cluster, we

183 generated an immune activation (IA) score based on the relative expression of a curated set of

184 41 genes known to have major roles in tumor cell-intrinsic immune functions, such as regulation

185 of MHC expression, antigen processing and presentation, NK cell recognition and T and NK cell

186 infiltration **(Supplementary Table 3)**. After assigning an IA score to each of the *MYCN-*

187 nonamplified tumors (n = 401) in the SEQC-498 data set and arranging them in ascending order

188 **(Supplementary Table 4),** we observed that a significant number with the highest IA scores

189   predominantly fell within the immunogenic and metabolic clusters **(Fig. 1e; Supplementary Fig.**

190   **2a)**, while those with intermediate or lower scores were associated with the neuronal and Hi-

191   MYCN clusters, respectively **(Fig. 1e; Supplementary Fig. 2a)**. Because a cytotoxic immune

192   response is generally accompanied by immune suppression or evasion[35,36], we determined

193   whether immune suppression was also represented in the *MYCN*-nonamplified tumors by ranking

194   them in ascending order of an immune evasion (IE) score based on the relative expression of 19

195   genes, most of which were markers of T-cell dysfunction **(Supplementary Table 3)**. Again, the

196   immunogenic tumor cluster had significantly higher IE scores compared with the neuronal and

197   metabolic clusters **(Fig. 1f; Supplementary Fig. 2b).** Moreover, we observed enrichment for IA

198   and IE scores in the immunogenic cluster in the additional data set (GSE120572)

199   **(Supplementary Fig. 2c),** thus strengthening our premise that these tumors maybe capable of

200   eliciting an immune response.

201

202   Consistent with the known poor immunogenicity of *MYCN*-amplified tumors[24,25], we also

203   observed that tumors within the Hi-MYCN cluster had, on the whole, the lowest IA and IE scores

204   **(Supplementary Fig. 2a, b).** Surprisingly, however, a small subset within this cluster had scores

205   that were comparable to the highly immunogenic tumors within the immunogenic cluster [13 of

206   103 (12.6%) above the median for immunogenic tumors] **(Supplementary Fig. 2a, b**). Thus, while

207   the majority of neuroblastomas do not possess an immune response gene signature, a subset

208   has significantly increased expression of both immune activation and evasion markers, pointing

209   to their ability to induce an anti-tumor immune response.

210

211   **The mesenchymal lineage is preferentially associated with immune response signatures**

212   **in neuroblastoma**

213   Having identified subsets of neuroblastomas with the potential for immunogenicity, we next sought

214   a biomarker that might consolidate the complex interactions between the immune system and the

215   tumor. To this end, we performed a modular gene co-expression analysis of the 140

216   transcriptomes within the immunogenic cluster in the SEQC-498 data set to identify biologically

217   relevant pathways based on similar gene expression patterns. Using the CEMiTool (co-

218   expression modules identification tool) package (Russo et al., 2018), we identified five gene co-

219   expression modules (M1-M5) within the immunological cluster **(Supplementary Fig. 3a).** Among

220   these modules, M1, with the highest number of co-expressed genes, contained gene sets

221   enriched for epithelial to mesenchymal transition (EMT), inflammatory response, and interferon

222   signaling, suggesting an association between EMT and the preponderant representation of

223   immune marker genes within the immunogenic cluster **(Fig. 2a; Supplementary Fig. 3b**).

224   Furthermore, integration of the co-expression data in module M1 with protein–protein interaction

225   data from the STRING 11.0 database identified mesenchymal lineage and immune markers as

226   top regulatory hubs **(Fig. 2b)**, leading us to hypothesize that in neuroblastoma, tumor

227   immunogenicity could be determined by cell state.

228

229   Two independent groups [37,38] recently described two distinct cell states in neuroblastoma: a

230   differentiated sympathetic neuron-like adrenergic (ADR) phenotype, defined by lineage markers

231   including *PHOX2B, DBH,* and *TH*, and a mesenchymal (MES) phenotype, characterized as

232   "neural crest cell-like" (NCC), and expressing genes such as *PRRX1, FOSL1,* and *FOSL2*. To

233   test our prediction, we first quantified the adrenergic and mesenchymal identities of each tumor

234   in our cohort based on the expression levels of the lineage-specific genes in each cell state as

235   established by Groningen et al[38] (see Methods). We ensured that there was no overlap between

236   the 369-gene adrenergic signature and the genes that made up the IA data set and removed the

237   6 IA genes that were also present in the 485-gene mesenchymal signature. Next, we assigned

238   either an adrenergic (A-score) or a mesenchymal (M-score) score to each tumor within our four

239   previously identified clusters. This analysis revealed significant enrichment of the mesenchymal

240   cell state within the immunogenic and metabolic clusters **(Fig. 2c; Supplementary Fig. 3c)**.

Fig. 2.
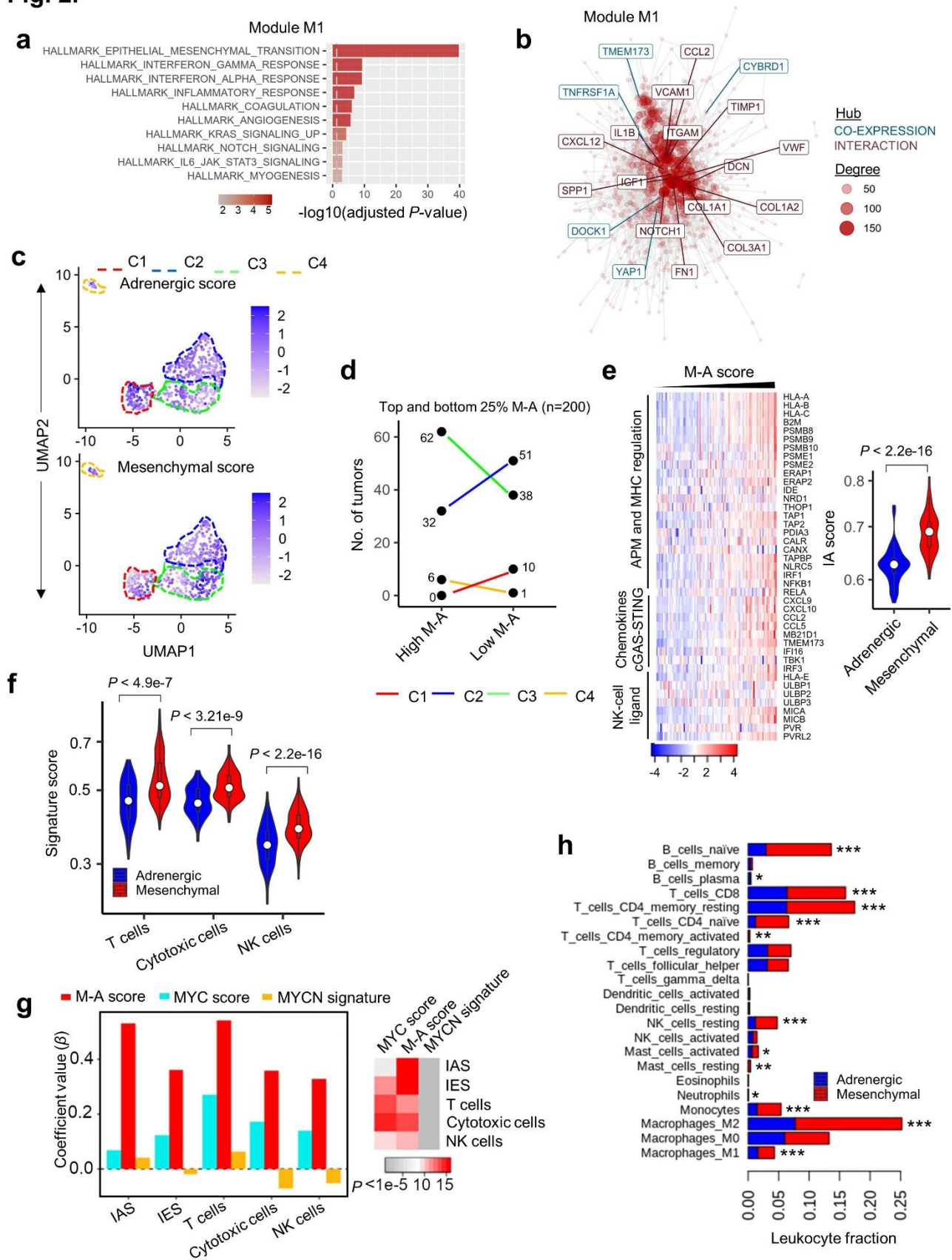
241 **Fig. 2. The mesenchymal cell state is associated with an immunogenic signature in NB. (a)**

242 GO analysis of co-expressed genes associated with module M1 using the KEGG (Kyoto

243 encyclopedia of genes and genomes) database. The vertical dashed line indicates the adjusted

244 *P*-value of 0.05. **(b)** Gene network representing all possible interactions in module M1. The

245 topmost connected genes (hubs) are indicated. Hubs derived from module M1 are colored blue

246 (co-expression) and those from the STRING database are indicated in red (interaction). The size

247 of each node corresponds to the degree of interaction. **(c)** UMAP visualization of the distribution

248 of adrenergic (top) and mesenchymal scores (bottom) among the four tumor clusters. Color bar

249 represents normalized z-scores. Values <2.5 and >2.5 were set to -2.5 and +2.5 respectively, to

250 reduce the effects of extreme outliers. **(d)** Dot plots showing the distribution of *MYCN-*

251 nonamplified tumors (n = 400) within each of the clusters based on ranked M-A scores. *Left*,

252 Tumors from the upper (high M-A) and lower (low M-A) M-A score quartiles are shown (n = 200;

253 *P* < 0.01 for C3). *Right*, Representations based on the median M-A scores of the entire tumor

254 cohort (n = 400; *P* = 0.05 for C3). Fisher's exact test was used for both calculations. **(e)** *Left*,

255 Heatmap representation of the expression of tumor cell-intrinsic immune activation genes in

256 *MYCN*-amplified tumors (n=92). Samples are ranked by increasing M-A score. Log$_2$ gene

257 expression values were z-score transformed for heatmap visualization. *Right*, Violin plots of the

258 distribution of immune activation scores in the tumors on the left, classified either as adrenergic

259 or mesenchymal, based on the median M-A score. The box plots within the violin plots are defined

260 by center lines (medians), box limits (25th and 75th percentiles), whiskers (minima and maxima;

261 1.5X the interquartile range). Significance was determined by the two-sided Kolmogorov-Smirnov

262 (KS) test. APM, antigen processing machinery. **(f)** Violin plots comparing the quantitative scores

263 of the indicated immune cell signatures in 100 tumors from the upper (mesenchymal) and lower

264 (adrenergic) quartiles of the tumor M-A scores using the two-sided KS test. The box plots within

265 the violin plots are defined as in (D). **(g)** *Left*, Bar diagram comparing regression coefficient (*β*)

266 values derived from multivariate multiple regression model analysis of *MYCN*-nonamplified

267   tumors. *β*-coefficient values were compared between three predictors: MYC score, M-A score and

268   MYCN signature. IA, IE, T cell, cytotoxic cell and NK cell scores were used as response variables

269   to generate the model[39]. *Right,* Heat map of the *P*-values associated with the three predictors. **(h)**

270   Bar diagram comparing the CIBERSORT-estimated fractional content of the indicated tumor-

271   infiltrating leukocytes between *MYCN*-nonamplified adrenergic and mesenchymal tumors.

272   Adrenergic and mesenchymal tumors were assigned as in **(f)**. Data represent the means, n = 100

273   tumors, *$P < 0.05$, **$P < 0.01$, ***$P < 0.001$ two-tailed Welch's t-test.

Supplementary Fig. 3.
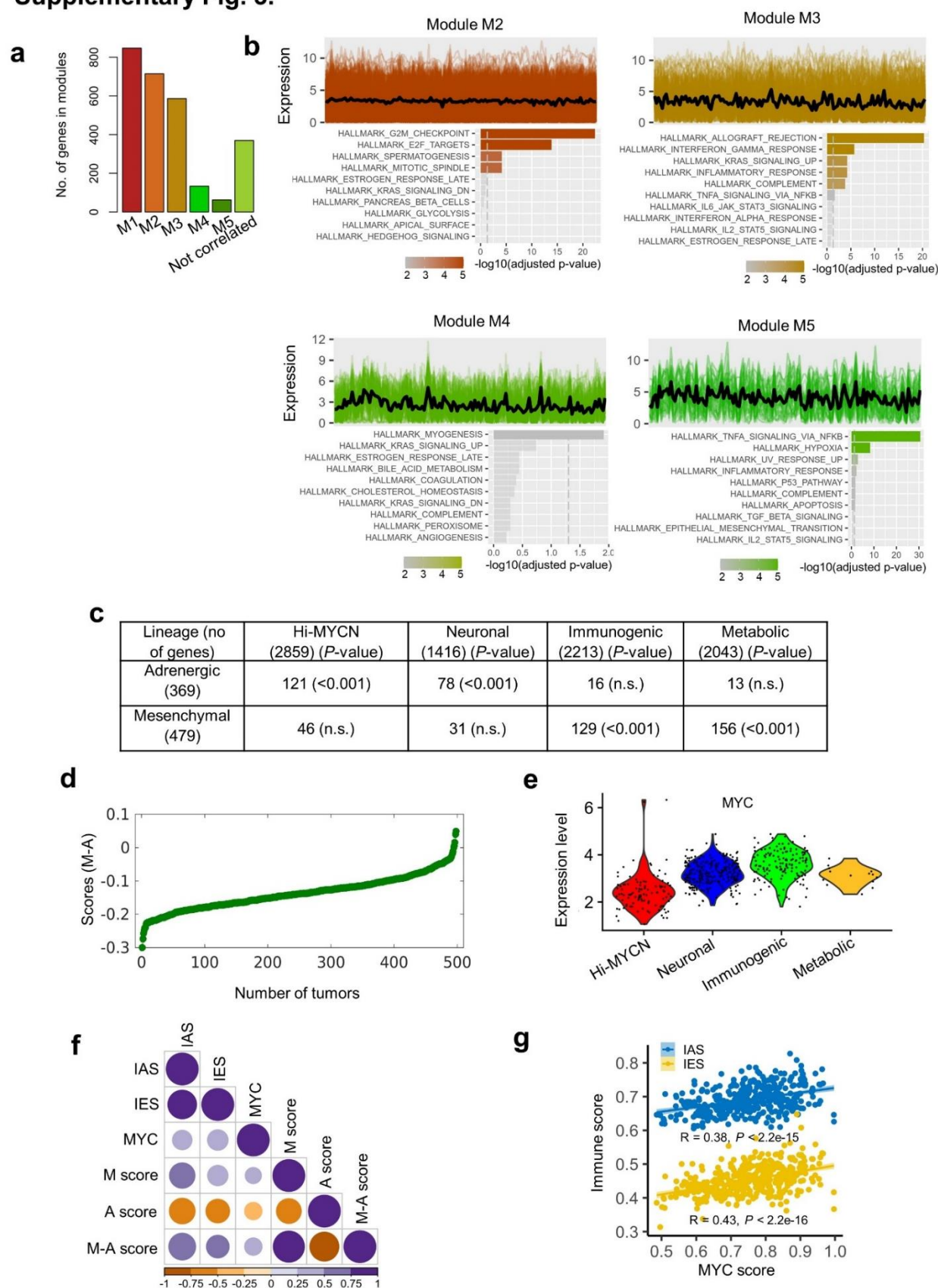
274   **Supplementary Fig. 3. Cell lineage markers are significantly associated with immune gene**

275   **signatures in NB. (a)** Bar plots representing the numbers of co-expressed genes within each

276   module. **(b)** Profile plots depicting the expression levels (y-axis) of individual genes (colored lines)

277   and their mean expression (black line) in 140 tumors (x-axis) from modules M2, M3, M4 and M5.

278   GO analysis of co-expressed genes associated with each module using the KEGG database is

279   appended below the respective profile plot. The vertical dashed line indicates the adjusted *P-*

280   value of 0.05. **(c)** Summary of the overlap between the DEGs associated with the four tumor

281   clusters and the adrenergic or mesenchymal signature genes as per Groningen et al., 2017.

282   Significance was determined by Fisher's exact test. **(d)** Scatter plot of the 498 primary NB tumors

283   ranked based on increasing M-A score. **(e)** Violin plots of the distribution of normalized expression

284   levels of MYC in the four tumor clusters. **(f)** Pearson correlation matrix showing pairwise

285   correlation values among the indicated parameters. The colors and sizes of the circles indicate

286   the correlation coefficient values, with the least (smaller, orange circles) to the most (larger, blue

287   circles) degree of association between the parameters shown. **(g)** Scatter plot of the correlation

288   between MYC expression and immune activation (blue dots) or evasion (yellow dots) scores in

289   *MYCN*-nonamplified tumors.

290

Supplementary Fig. 4.

a

b

c

d

e
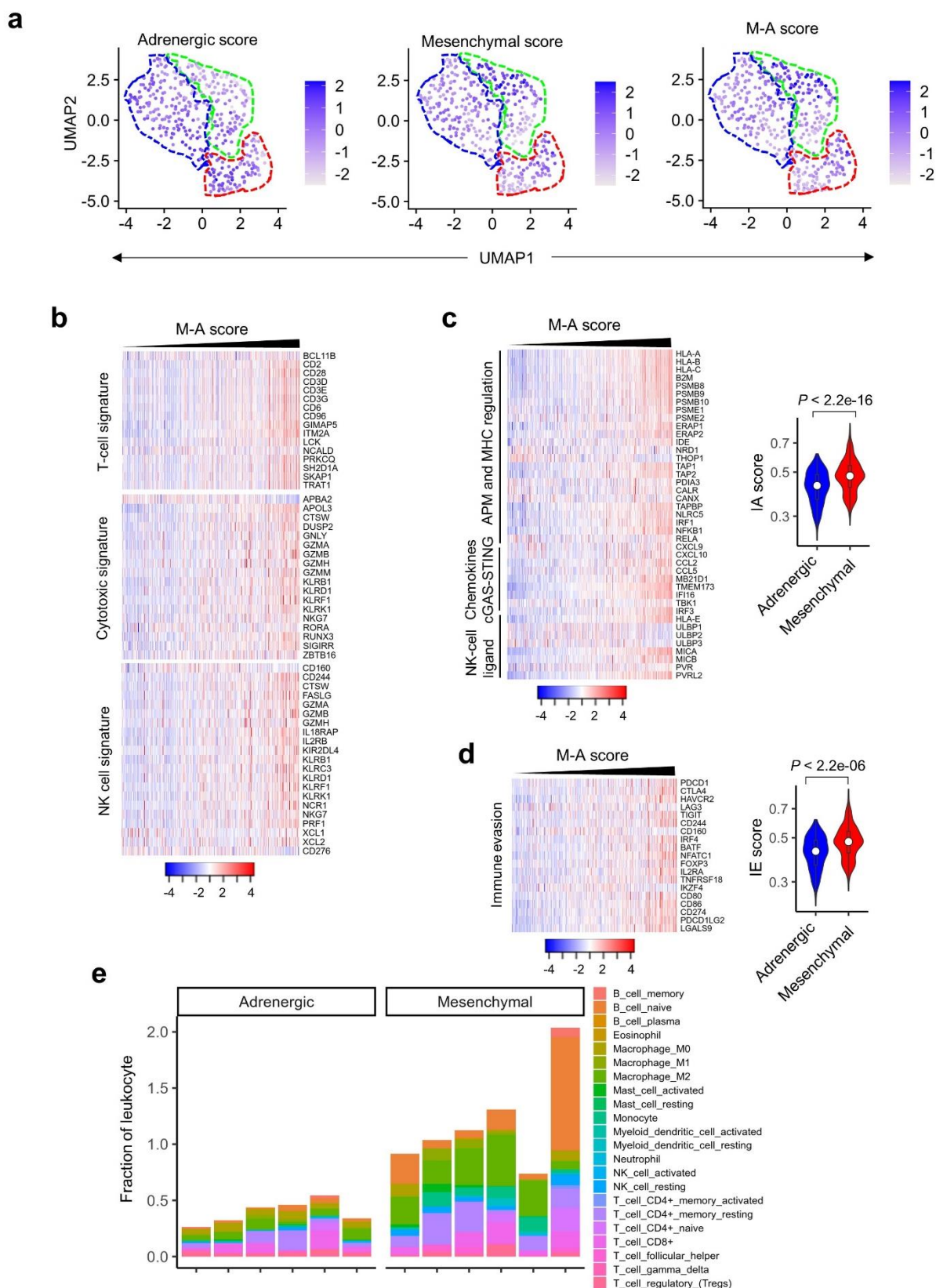
291 **Supplementary Fig. 4. The relative mesenchymal score (M-A score) is positively correlated**

292 **with an immunogenic signature. (a)** UMAP visualization of the distribution of adrenergic,

293 mesenchymal, and M-A scores among the three tumor clusters derived from 394 NBs in the

294 GSE120572 dataset. Color bar represents normalized z-scores. Values <2.5 and >2.5 were set

295 to -2.5 and +2.5 respectively, to reduce the effects of extreme outliers. **(b)** Heat maps of the

296 indicated immune cell signatures in *MYCN*-nonamplified tumors, ranked by increasing M-A

297 scores. Log$_2$ gene expression values were z-score transformed for heatmap visualization. **(c, d)**

298 Heatmaps depicting the immune activation **(c)** and evasion **(d)** signatures in *MYCN*-nonamplified

299 tumors, ranked by increasing M-A score. Log$_2$ gene expression values were z-score transformed

300 for visualization. Violin plots comparing the distribution of immune activation **(c)** and evasion **(d)**

301 signatures in 100 tumors from upper (mesenchymal) and lower (adrenergic) quartiles of the M-A

302 score are shown next to the heatmaps. Significance determined by the two-sided KS test. Box

303 plots within the violin plots are defined by center lines (medians), box limits (25th and 75th

304 percentiles), whiskers (minima and maxima; 1.5X the interquartile range). **(e)** Bar graph

305 comparing the CIBERSORT-estimated fractional content of the indicated tumor-infiltrating

306 leukocytes in six tumors with the uppermost (mesenchymal) and lowermost (adrenergic) M-A

307 scores.

308   By contrast, the Hi-MYCN and neuronal clusters were enriched for the adrenergic cell state **(Fig.**

309   **2c; Supplementary Fig. 3c)**.

310   Next, to identify predictors of immunogenicity among the *MYCN*-nonamplified tumors, we

311   calculated the relative mesenchymal score for each tumor by subtracting the adrenergic from the

312   mesenchymal score (M-A score). This resulted in a continuum of low to high M-A scores,

313   corresponding to a less mesenchymal to a more mesenchymal tumor state **(Supplementary Fig.**

314   **3d)**. To determine whether these cell states had any effect on immune response in the *MYCN*-

315   nonamplified tumors, we determined whether the mesenchymal, adrenergic, or M-A scores

316   correlated with our previously defined immune activation and evasion scores **(Fig. 1e, f)**. We also

317   tested the effect of *MYC*, one of the top differentially expressed genes in the immunogenic cluster

318   **(Supplementary Fig. 3e)**. *MYC* is overexpressed in approximately 10% of *MYCN*-nonamplified

319   neuroblastomas[40] and regulates the expression of cell-intrinsic immune evasion markers in

320   lymphoma[41]. Of these variables, the M-A score showed the strongest correlation with

321   immunogenicity, not only in terms of the immune activation score (R = 0.71), but also the immune

322   evasion score (R = 0.51) **(Supplementary Fig. 3f)**. MYC expression was only modestly correlated

323   with immune evasion and activation scores (R = 0.43; R= 0.38, respectively) **(Supplementary**

324   **Fig. 3g)**. With no overlap between the lineage marker and immune response gene sets, these

325   results suggest that the relative abundance of a mesenchymal signature (M-A score) is a better

326   predictor of immune response than individual adrenergic or mesenchymal signatures.   In

327   agreement, tumors with high M-A scores were represented at a significantly higher proportion

328   within the immunogenic cluster compared to tumors with low M-A scores **(Fig. 2d),** a result that

329   was recapitulated in our second data set, (GSE120572) **(Supplementary Fig. 4a)**. Finally, our

330   finding of the subset of tumors marked by the relatively high expression of immune activation and

331   evasion genes within the Hi-MYCN cluster (**Supplementary Fig. 2a, b)** prompted us to further

332   evaluate the cell states of these tumors. Ranking these tumors based on increasing M-A scores

333   revealed a positive relationship between cell-intrinsic immunogenicity and the mesenchymal state

.

.

334 **(Fig. 2e)**, suggesting that similar to our results in *MYCN*-nonamplified tumors, the presence of

335 immune gene expression in *MYCN*-amplified tumors is significantly correlated with the

336 mesenchymal phenotype.

337

338 The preferential overexpression in the mesenchymal phenotype of tumor cell-intrinsic genes

339 that induce a positive immune response (IA score), as well as its correlation with transcripts that

340 suppress the immune response (IE score), suggested that these tumors may support increased

341 immune cell infiltration**.** To test this prediction, we used two orthogonal approaches. First, we

342 assessed whether established signatures of immune cell infiltration [39,42] were present in the

343 tumors arranged according to increasing M-A scores, and observed enrichment for signatures of

344 infiltrating immune cells in tumors with mesenchymal phenotypes **(Supplementary Fig. 4b)**.

345 Intriguingly, we also noted that adrenergic tumors were enriched for CD276 (B7-H3) expression,

346 an immune checkpoint marker that protects neuroblastoma cells from NK cell-mediated

347 cytotoxicity, which may partly account for the decreased immune response signatures in these

348 cells[14] **(Supplementary Fig. 4b).** We next quantified the immune response signatures in a subset

349 of tumors (n = 100) from both the upper and lower quartiles of the M-A score that had significant

350 differences in their activation and evasion scores **(Supplementary Fig. 4c, d)**. High M-A scoring

351 (mesenchymal) tumors had significantly higher expression levels of cytotoxic T and NK cell

352 signatures compared with those of low M-A scoring (adrenergic) tumors (**Fig. 2f**). Considering

353 that the M-A score and, to a lesser extent, higher *MYC* expression were positively associated with

354 IA and IE scores in pairwise testing **(Supplementary Fig. 3f)**, we next assessed their relative

355 contributions as independent predictors of an immune response in a multivariate multiple

356 regression model consisting of immune activation and evasion scores and T and NK cell

357 signatures **(Fig. 2g)**. Because *MYCN* amplification is linked to immune suppression, we also

358 included the 157-gene *MYCN* signature generated by Valentijn et al[27] and subsequently used by

359 Wei et al to identify immune predictors in *MYCN*-nonamplified neuroblastoma[25]. In this analysis

360   also, the M-A score was a better predictor of tumor immunogenicity than *MYC* expression or

361   *MYCN* signature **(Fig. 2g)**.

362

363   Second, we used CIBERSORT (Cell type Identification By Estimating Relative Subsets Of

364   known RNA Transcripts)[43], as a deconvolution approach to estimate the fraction of immune cell

365   infiltration associated with the adrenergic and mesenchymal lineage tumors. We first established

366   the fraction of tumor-infiltrating leukocytes (TILs) in the most mesenchymal versus the most

367   adrenergic tumors (n = 6 each), observing significantly higher fractions in mesenchymal tumors

368   **(Supplementary Fig. 4e).** Next, we quantified the average immune cell content in 100 tumors

369   from the upper and lower quartiles of the M-A score **(Fig. 2h)**. Consistent with our previous results

370   **(Fig. 2f)**, CIBERSORT analysis also showed significantly increased enrichment for cytotoxic CD8^{+}

371   T cells in mesenchymal tumors, which was also associated with a concomitant increase in

372   regulatory T cells, including those expressing markers of T-cell exhaustion **(Fig. 2h;**

373   **Supplementary Fig. 4e)**. Interestingly, we also observed that mesenchymal tumors comprised a

374   higher fraction of naïve B cells, which were recently shown to take part in antitumor immunity [44]

375   **(Fig. 2h; Supplementary Fig. 4e)**. Together, our findings indicate that the mesenchymal cell

376   state is a strong predictor of neuroblastoma immunogenicity.

377

378   **Tumor cell-intrinsic upregulation of immune pathways in mesenchymal neuroblastoma**

379   We next sought to understand the extent to which the presence or absence of an immunogenic

380   signature in the bulk RNA-sequencing data was intrinsic to tumor cells or was conferred by the

381   tumor microenvironment. Analysis of the lineage identities of a panel of 24 human neuroblastoma

382   cell lines (15 *MYCN*-amplified; 9 *MYCN*-nonamplified) from RNA-sequencing data (GSE28019)

383   revealed a gradient of adrenergic-to-mesenchymal scores **(Supplementary Fig. 5a)**. Consistent

Fig. 3.
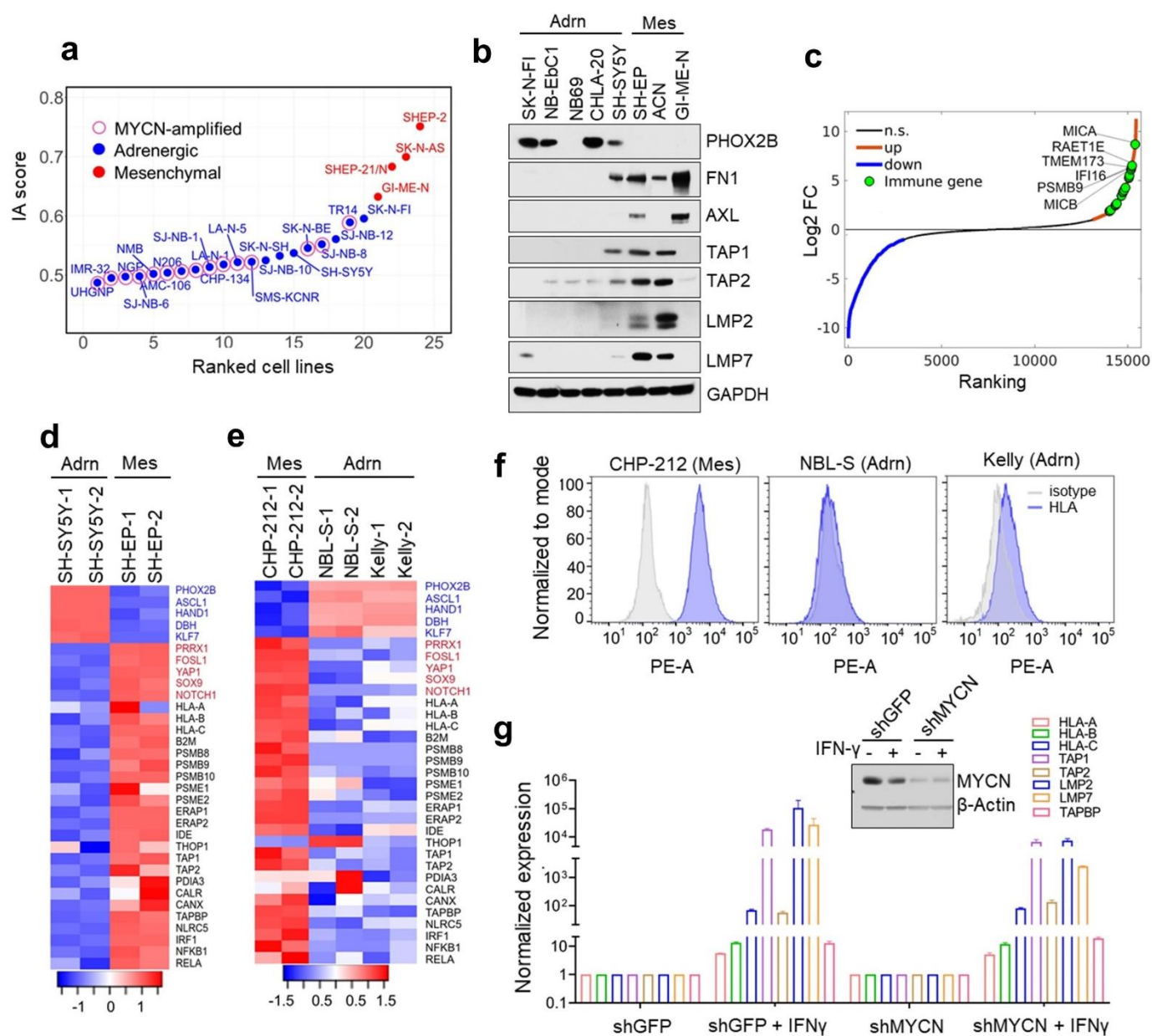
384 **Fig. 3. Tumor cell-intrinsic immune marker genes are upregulated in mesenchymal NBs.**

385 **(a)** Scatter plot of the immune activation (IA) scores of human neuroblastoma cell lines (RNA-seq

386 data; GSE28019). Cell lines are arranged based on increasing IA scores and designated as

387 adrenergic or mesenchymal based on lineage-specific gene expression. **(b)** Western blot (WB)

388 analysis of adrenergic (PHOX2B) and mesenchymal (FN1, AXL) cell lineage markers and antigen

389 processing genes (TAP1/2, LMP2/7) in *MYCN*-nonamplified NB cell lines. GAPDH was used as

390 the loading control. Adrn, adrenergic; Mes, mesenchymal. **(c)** Waterfall plot of the fold-change in

391 RNA expression levels of up- and downregulated genes in SH-EP compared to SH-SY5Y NB

392 cells; selected immune genes are highlighted in green. **(d, e)** Heat maps of lineage marker (*blue*,

393 adrenergic; *red*, mesenchymal) and MHC and antigen processing machinery gene (*black*)

394 expression in the indicated *MYCN*-nonamplified **(d)** and *MYCN*-amplified (CHP-212, Kelly) and

395 overexpressing (NBL-S) **(e)** adrenergic and mesenchymal cells ($n = 2$ biological replicates). Rows

396 are z-scores calculated for each transcript in each cell type. **(f)** Fluorescence activated cell sorting

397 (FACS) analysis of cell surface HLA expression in the cells depicted in **e**. Isotype controls are

398 depicted in gray. The X-axis denotes fluorescence intensity of indicated proteins using

399 phycoerythrin (PE-A) tagged antibodies. Results representative of 2 independent experiments.

400 **(g)** RT-qPCR analysis of antigen processing and presentation genes in *MYCN*-amplified Kelly NB

401 cells engineered to express shMYCN or shGFP (control) with or without IFN-γ induction (100

402 ng/mL for 24 hr.). Data are normalized to GAPDH and represent means ± SD, $n = 2$ biological

403 replicates. Inset, WB analysis of MYCN in control and shMYCN cells. Actin was used as a loading

404 control.

Supplementary Fig. 5.

a

b

c

e

d

f
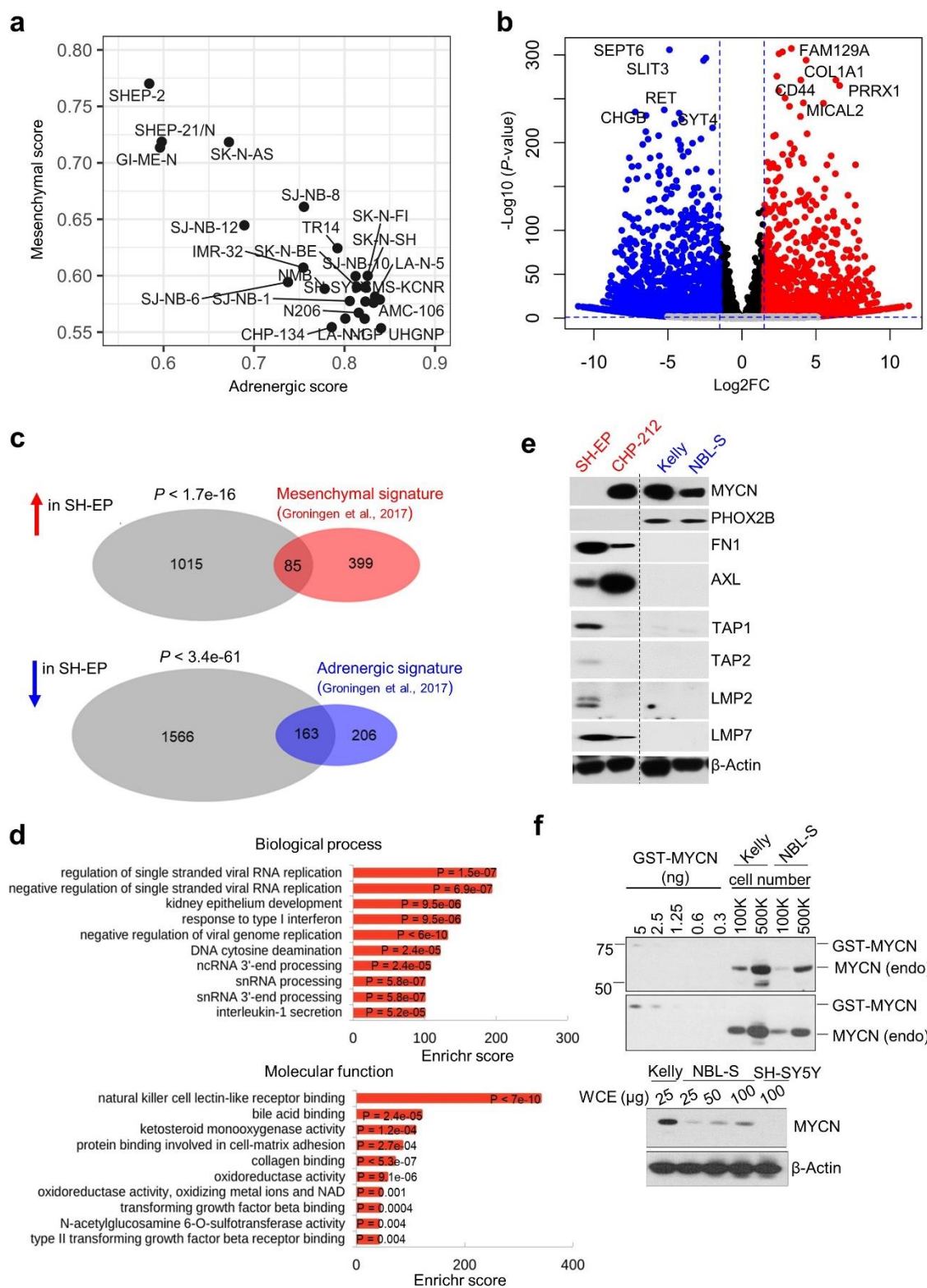
405 **Supplementary Fig. 5. Mesenchymal lineage-specific marker and cell-intrinsic immune**

406 **gene expression are significantly correlated in NB.** **(a)** Scatter plot of adrenergic and

407 mesenchymal scores in NB cell lines (GSE28019). **(b)** Volcano plot showing the gene expression

408 changes between mesenchymal SH-EP and adrenergic SH-SY5Y cells. The top ten lineage

409 marker genes are highlighted. The fold changes are represented in $\log_2$ scale (X-axis) and the -

410 $\log_{10}$ of the *P*-values depicted on Y-axis (FDR < 0.1 and $\log_2$FC > 1). **(c)** Venn diagram of the

411 overlap between DEGs in SH-EP cells (compared to SH-SY5Y cells) and the mesenchymal or

412 adrenergic signatures derived from Groningen et al[38]. Statistical significance was determined

413 using Fisher's exact test. **(d)** GO analysis of differentially upregulated genes in mesenchymal SH-

414 EP compared to adrenergic SH-SY5Y cells. **(e)** WB analysis of cell lineage marker and antigen

415 processing gene expression in the indicated NB cells. Dotted line indicates the margin where gel

416 images have been cut. **(f)** *Upper*, WB analysis of MYCN levels in the indicated numbers of Kelly

417 and NBL-S NB cells titrated against known amounts of purified GST-MYCN protein. *Lower,* WB

418 analysis comparing MYCN levels in whole cell extracts (WCE) from Kelly cells to titrated levels

419 from WCE in NBL-S cells. SH-SY5Y cells that do not express MYCN serve as a negative control.

420 Actin was used as a loading control in **(e)** and **(f)**.

421   with our observations in primary tumors, cell lines with higher mesenchymal gene signatures

422   grouped together and had significantly higher expression of tumor cell-intrinsic immune genes,

423   compared with the remainder, which had higher adrenergic scores and were mostly associated

424   with reduced immune marker gene expression (**Fig. 3a, b**). To further understand the association

425   of tumor cell-intrinsic immune pathways with lineage state, we focused on two neuroblastoma cell

426   lines –SH-SY5Y and SH-EP – subclones of the *MYCN*-nonamplified SK-N-SH cell line separated

427   on the basis of neuroblastic versus substrate-adherent morphology[45] and determined to be

428   adrenergic and mesenchymal[38], respectively. RNA sequencing showed that the differentially up-

429   and down-regulated genes in SH-EP compared with SH-SY5Y cells significantly overlapped with

430   established signatures of mesenchymal and adrenergic states, thus confirming their respective

431   phenotypes **(Supplementary Fig. 5b, c).** We noted that genes with roles in eliciting an immune

432   response were among the top differentially upregulated genes in mesenchymal SH-EP cells,

433   especially those involved in antigen processing and presentation and positive regulation of MHC

434   expression **(Fig. 3c, d)**. Moreover, gene ontology (GO) analysis of the upregulated transcripts

435   revealed enrichment for innate and adaptive immune responses including type-I interferon

436   signaling and ligands for the NK cell receptor, NKG2D (NK cell lectin-like receptor, KLRK1)

437   **(Supplementary Fig. 5d)**. By contrast, adrenergic SH-SY5Y cells that showed upregulation of

438   neuronal lineage markers did not show significant enrichment of immune function genes **(Fig.**

439   **3d)**, providing further evidence that cell-intrinsic immunogenicity is associated with the

440   mesenchymal phenotype.

441   The absence of a productive immune response has often been described in *MYCN*-

442   amplified neuroblastoma tumors[24,25]; indeed, the vast majority of such tumors in our cohort

443   exhibited similar findings **(Supplementary Fig. 2a, b)**. Nonetheless, based on our intriguing

444   finding of upregulation of immune response genes in a small number of *MYCN*-amplified tumors

445   **(Supplementary Fig. 2a, b)** that possessed mesenchymal cell signatures **(Fig. 2e)**, we sought

446   to understand the role of MYCN in mediating this immune response. We used Kelly and CHP-212

447   human neuroblastoma cells that expressed amplified *MYCN* but were of adrenergic and

448   mesenchymal phenotypes, respectively[37,38], and NBL-S cells that lacked *MYCN* amplification but

449   expressed moderate levels of MYCN RNA and protein[46] **(Supplementary Fig. 5e)** and were

450   classified as adrenergic (van Groningen et al., 2017 and this study). RNA-sequencing and flow

451   cytometry analysis suggested that tumor cell-intrinsic immune genes involved in antigen

452   processing and MHC regulation were highly expressed in mesenchymal CHP-212 compared to

453   adrenergic Kelly and NBL-S cells **(Fig. 3e, f; supplementary fig. 5e)**. Importantly, although

454   MYCN expression in NBL-S cells was lower than in Kelly cells **(Supplementary Fig. 5f)**, these

455   immune transcripts were expressed at lower levels in both cell lines, consistent with their

456   adrenergic status **(Fig. 3e; Supplementary Fig. 5f).** To further verify that cell state dictate tumor

457   cell-intrinsic immunogenicity, we depleted MYCN expression in Kelly cells and observed no

458   significant change to the IFN-γ-induced expression of HLA and antigen processing genes

459   compared to control cells **(Fig. 3g)**. Thus, our findings suggest that the lineage state of

460   neuroblastoma cells specifies the expression of tumor cell-intrinsic immune marker genes.

461

462   **Cellular reprogramming to the mesenchymal state leads to increased immunogenicity**

463   We next questioned whether acquisition of the mesenchymal phenotype would be sufficient to

464   render adrenergic neuroblastoma cells immunogenic. One of the top overexpressed genes in SH-

465   EP mesenchymal cells, *PRRX*1, encodes a core lineage-specific homeobox transcription factor

466   (TF), whose overexpression induces the mesenchymal state in neuroblastoma cells[37,38]

467   **(Supplementary Fig. 5b)**. We therefore overexpressed doxycycline-inducible *PRRX1* in

468   adrenergic SH-SY5Y cells and observed a gradual loss of the adrenergic lineage marker

469   PHOX2B, together with increased expression of the mesenchymal markers, fibronectin, vimentin

470   and AXL **(Fig. 4a; Supplementary Fig. 6a)**. By contrast, overexpression of DNA-binding mutants

Fig. 4.
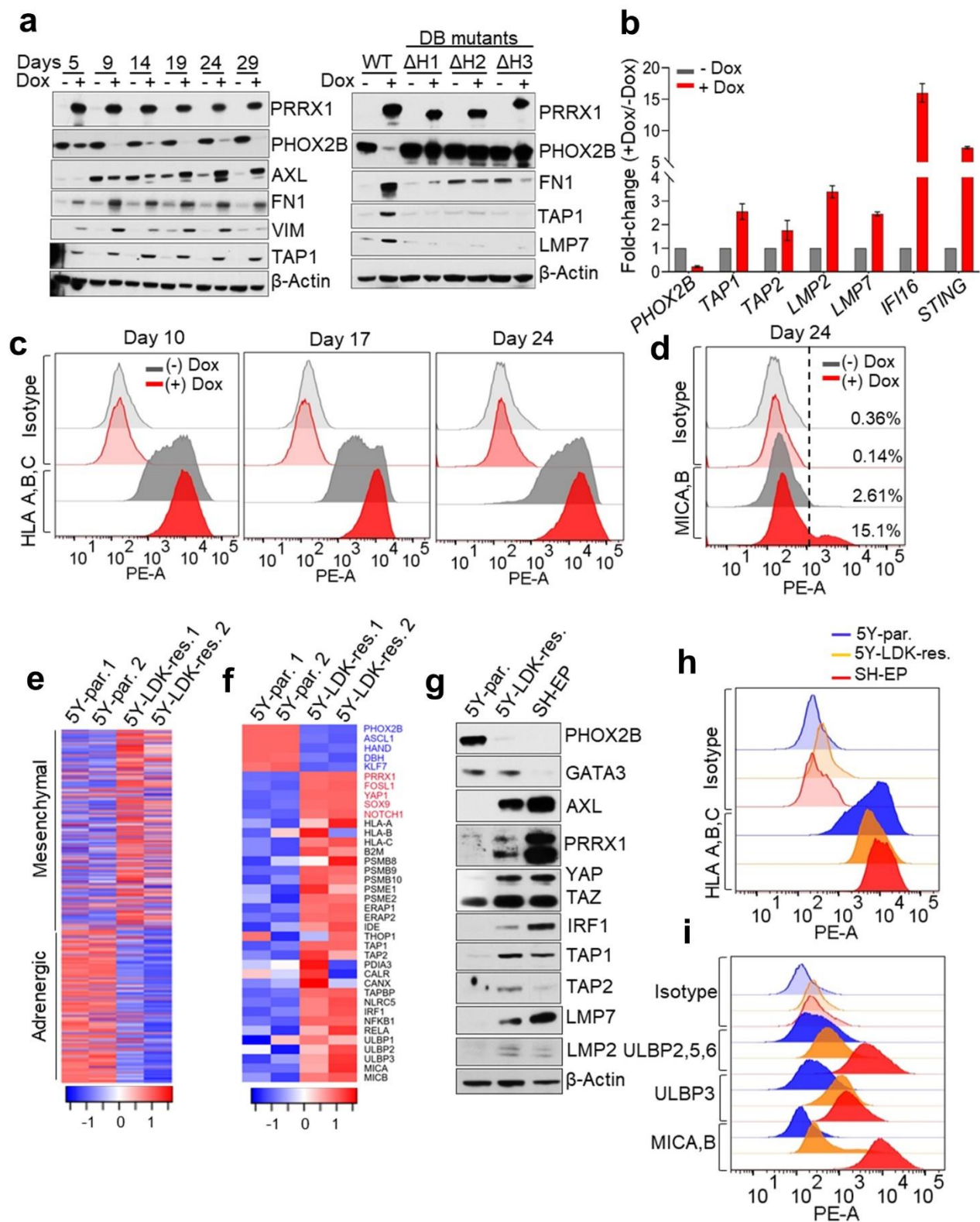
471 **Fig. 4. Reprogramming of adrenergic NB cells to the mesenchymal cell state leads to**

472 **increased expression of immune response genes. (a)** *Left*, WB analysis of PHOX2B and

473 antigen processing gene expression in adrenergic SH-SY5Y cells engineered to express

474 doxycycline (dox)-inducible PRRX1 in the presence or absence of dox (200 ng/mL) at the

475 indicated time points. *Right*, WB analysis of the indicated proteins in SH-SY5Y cells expressing

476 dox-inducible wild-type (WT) or DNA-binding mutants of PRRX1 at 10 days post dox-induction.

477 The DNA-binding (DB) mutants harbor individual deletions of the three α-helices (ΔH1, ΔH2 and

478 ΔH3) within the PRRX1 homeodomain. **(b)** RT-qPCR analysis of the indicated immune response

479 genes in the same cells as in **(a).** Data represent the means ± SD, *n* = 2 biological replicates. **(c)**

480 FACS analysis of cell surface HLA expression following dox-inducible expression of PRRX1 in

481 SH-SY5Y cells at the indicated time points. Data are representative of 2-3 independent

482 experiments. **(d)** FACS analysis of cell surface MICA/MICB expression after PRRX1 induction for

483 24 days in the same cells as in **(c).** A logscale expression value of 10^3 was used as a threshold

484 (vertical line) to gate MICA/MICB negative ($<10^3$) and positive ($\geq10^3$) populations. Numbers on

485 the right indicate the percentage of MICA/MICB-positive cells. Plots are representative of 2

486 independent experiments. **(e)** Heat map representation of adrenergic and mesenchymal gene

487 signatures in parental (5Y-par) and LDK-resistant (5Y-LDK-res) SH-SY5Y cells (*n* = 2 biological

488 replicates). Rows represent z-scores of $\log_2$ expression values for each gene in both cell types.

489 **(f)** Heat map depicting the expression of cell lineage markers (blue, adrenergic; red,

490 mesenchymal), antigen processing machinery genes and NKG2D ligands (black) in parental and

491 LDK-resistant SH-SY5Y cells (*n* = 2 biological replicates). Rows represent z-scores of $\log_2$

492 expression values. **(g)** WB analysis of lineage marker and antigen processing gene expression in

493 the indicated cells. Actin was used as a loading control in all immunoblots. **(h, i)** FACS analysis

494 of cell surface HLA **(h)** and NKG2D ligand **(i)** expression in the indicated cells.

Supplementary Fig. 6.

a

PRRX1

b

c

d

e
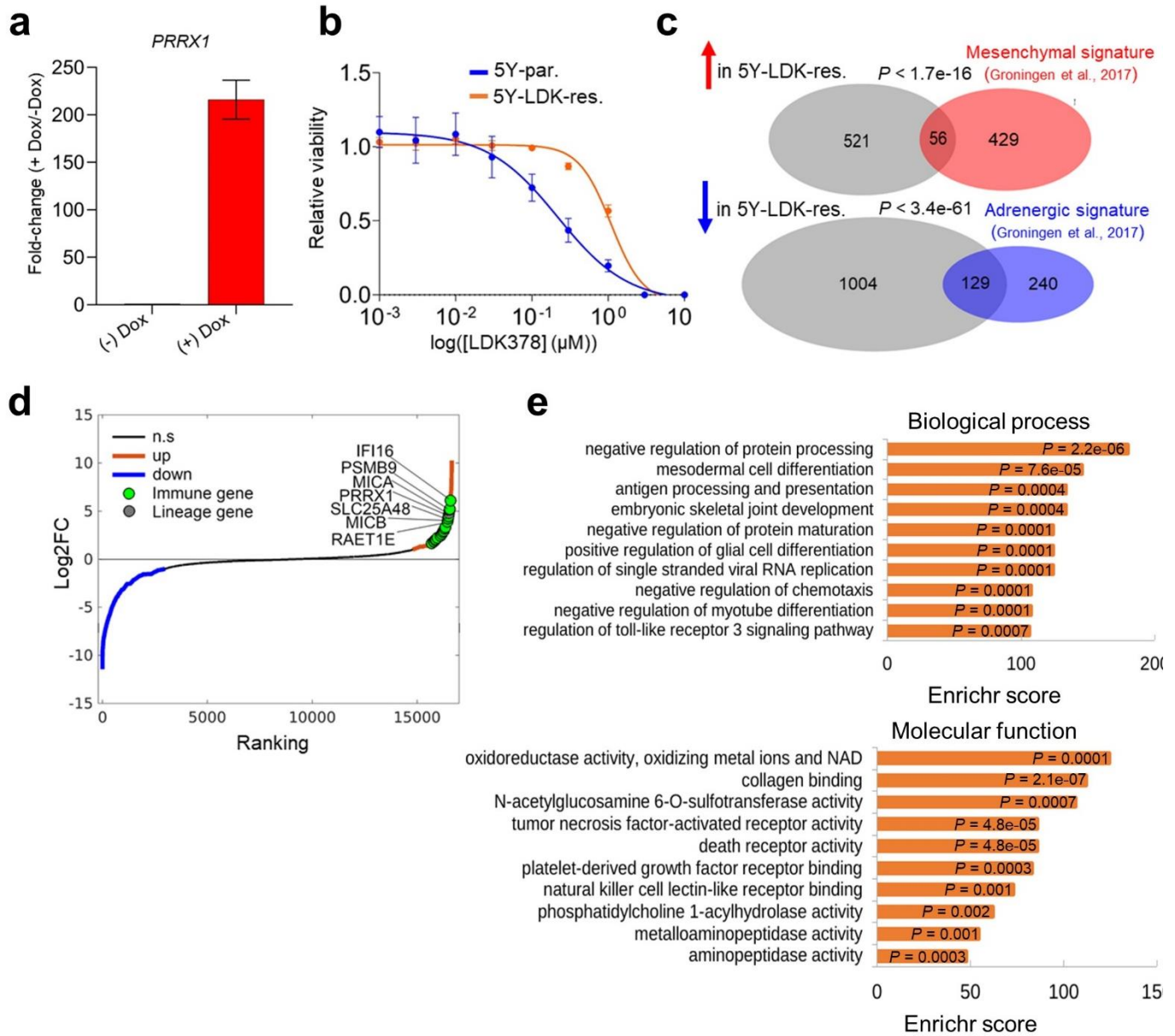
496 **Supplementary Fig. 6. Acquired resistance to ceritinib (LDK387) in adrenergic SH-SY5Y**

497 **cells is associated with reprogramming to the mesenchymal lineage and increased**

498 **expression of immune response genes.** **(a)** RT-qPCR analysis of PRRX1 expression in

499 adrenergic SH-SY5Y cells engineered to express doxycycline (dox)-inducible PRRX1 in the

500 presence or absence of dox (200 ng/mL) for 10 days. Data represent the means ± SD, n = 2

501 biological replicates. **(b)** Dose–response curves of ceritinib (LDK378)-sensitive (5Y-par.) and -

502 resistant (5Y-LDK-res.) SH-SY5Y cells treated with increasing concentrations of LDK378 for 72

503 h. Data represent means ± SD, n = 2 biological replicates. **(c)** Venn diagrams depicting the overlap

504 between the DEGs in LDK-resistant SH-SY5Y cells (compared to parental SH-SY5Y cells) and

505 the mesenchymal or adrenergic signatures derived from Groningen et al[38]. *P*-values were

506 determined by Fisher's exact test. **(d)** Waterfall plot of the fold-change in RNA expression levels

507 of up- and down-regulated genes in LDK-resistant SH-SY5Y cells compared to parental SH-SY5Y

508 cells; selected immune genes are highlighted in green. **(e)** GO analysis of differentially

509 upregulated genes in LDK-resistant SH-SY5Y compared to parental SH-SY5Y cells.

510   of *PRRX1* that contained homeodomain deletions had no effect on mesenchymal marker

511   expression, indicating that the lineage switch was a direct consequence of PRRX1-mediated

512   transcriptional control **(Fig. 4a)**. Next, to determine whether the phenotypic switch had any effect

513   on tumor cell-intrinsic pro-inflammatory pathways, we analyzed the expression of genes involved

514   in antigen processing (*TAP1, TAP2, LMP2, LMP7*) as well as *IFI16* and *STING* (*TMEM173*),

515   innate immune regulators that were differentially upregulated in mesenchymal NB cells **(Fig. 3c)**.

516   Induction of wild-type (WT) *PRRX1* led to increased RNA expression of these genes **(Fig. 4b)**.

517   Moreover, WT PRRX1 but not its DNA-binding mutants led to increased TAP1 and LMP7 protein

518   expression, which was accompanied by a sustained increase in cell surface MHC expression

519   **(Fig. 4a, c)**. Additionally, PRRX1 induction led to increased cell surface expression of MICA and

520   MICB, ligands for the activating NK cell receptor NKG2D, in a minor population of cells **(Fig. 4d)**,

521   in agreement with elevated expression of these proteins in mesenchymal neuroblastoma cells

522   **(Fig. 3c)**. These results suggest that conversion from the adrenergic to mesenchymal cell state

523   may be adequate to reprogram immune-insensitive cells toward immunocompetency.

524   Transition from the adrenergic to the mesenchymal state in neuroblastoma is

525   accompanied by resistance to chemotherapy [38]. Whether this transition in the face of treatment

526   pressure might include the acquisition of a pro-inflammatory signature is unclear, leading us to

527   compare adrenergic neuroblastoma cells that had gained mesenchymal features during the

528   development of treatment resistance with their sensitive, adrenergic counterparts. For this

529   purpose, we used an isogenic pair of cell lines comprising adrenergic SH-SY5Y neuroblastoma

530   cells that express the *ALK^{F1174L}* mutation and are sensitive to the small molecule inhibitor ceritinib

531   (LDK378) (parental SH-SY5Y, IC_{50} = 150 nM), and their ceritinib-resistant derivatives (LDK-

532   resistant SH-SY5Y, IC_{50} = 1101 nM) **(Supplementary Fig. 6b)**[47]. Comparison of the gene

533   expression signatures of these cell lines revealed significant downregulation of adrenergic

534   transcripts in LDK-resistant SH-SY5Y cells with concomitant upregulation of the mesenchymal

535   signature **(Fig. 4e)**. Moreover, a significant overlap was noted between the differentially up- or

536   downregulated transcripts in the LDK-resistant SH-SY5Y cells and established signatures of

537   mesenchymal and adrenergic states, respectively **(Supplementary Fig. 6c)**, suggesting that

538   these cells had acquired features of the mesenchymal phenotype with resistance. Consistent with

539   the key role of PRRX1 in triggering the conversion from an adrenergic to mesenchymal cell state,

540   we observed that this TF was among the top upregulated genes in LDK-resistant SH-SY5Y cells

541   **(Supplementary Fig. 6d).** The mesenchymal state of the LDK-resistant SH-SY5Y cells was

542   further supported by the loss of the pivotal adrenergic marker, PHOX2B, and increased

543   expression of additional mesenchymal markers AXL, YAP, TAZ, and IRF1, although these

544   changes were not as pronounced as those in SH-EP mesenchymal cells that served as a positive

545   control **(Fig. 4f, g)**. Further evidence supporting the conversion to the mesenchymal state came

546   from the differential upregulation in LDK-resistant SH-SY5Y cells of cell-intrinsic immune markers

547   engaged in antigen processing and presentation and NK cell activating receptor ligands (PSMB9,

548   MICA, MICB); in fact, these were among the top differentially upregulated genes in LDK-resistant

549   SH-SY5Y cells **(Supplementary Fig. 6d, e; Fig. 4f, g)**. These changes in immune genes

550   coincided with increases in cell surface expression of MHC receptors to levels comparable to

551   those in mesenchymal SH-EP cells **(Fig. 4h)**, as well as the increased expression of ligands for

552   the NK cell-activating receptor NKG2D **(Fig. 4i)**. Thus, the genetic reprogramming from the

553   adrenergic to the mesenchymal state that occurred with therapy resistance also led to the

554   upregulation of tumor cell-intrinsic pro-inflammatory pathway genes suggesting that such

555   conversion could render the tumor cells susceptible to recognition by T and NK cells.

556

Immune response gene expression during cell state transition is epigenetically regulated

557

558   As lineage plasticity in neuroblastoma is epigenetically driven[37,38,48,49], we next questioned

559   whether the altered expression of immune response genes observed in the individual cell states

560   could be the result of changes in chromatin organization. To this end, we analyzed the chromatin

561   occupancies of active and repressive histone marks at immune genes that were upregulated in

562   adrenergic SH-SY5Y cells upon induction of PRRX1 **(Fig. 4b)**. Indeed, PRRX1 induction resulted

563   in increased binding of the active H3K4me3 mark as well as loss of repressive H3K27me3 binding

564   at several candidate immune genes, including the APM genes *TAP1* and *PSMB9* **(Fig. 5a;**

565   **Supplementary Fig. 7a)**. To understand epigenetic modifications that occur during the

566   spontaneous transition between the two lineage states (as compared with forced expression of

567   *PRRXI*) on a genome-wide basis, we compared histone occupancies between adrenergic

568   (parental SH-SY5Y) cells and those that had acquired mesenchymal characteristics with drug

569   resistance (LDK-resistant SH-SY5Y) **(Fig. 4e),** using SH-EP cells as a typical example of the

570   mesenchymal state. ChIP-seq analysis of active H3K27ac binding identified that the super-

571   enhancers (SEs) in LDK-resistant SH-SY5Y cells were associated with genes that conferred

572   mesenchymal identity while parental SH-SY5Y cells retained SEs at genes that conferred

573   adrenergic identity **(Supplementary Fig. 7b),** consistent with evidence that lineage plasticity is

574   driven by cell type-specific SEs[37,38]. To determine whether the SE-mediated regulation of lineage

575   genes also extended to genes associated with immune responsiveness, we analyzed the genes

576   in our 41-gene immune activation signature **(Supplementary Table 3;Fig. 1e)** as well as those

577   associated with an IFN-response signature (n = 91) in primary tumors and cell lines **(Fig. 1b;**

578   **Supplementary Fig. 5d,** see Methods**)**. Despite the higher expression of these genes in

579   mesenchymal cells (LDK-resistant SH-SY5Y and SH-EP), none was associated with an SE,

580   prompting us to focus on the promoter regions. We observed significantly higher enrichment of

581   H3K27ac and H3K4me3 binding at regions spanning the transcription start sites (TSS ± 2 kb) at

582   cell-intrinsic immune genes in LDK-resistant SH-SY5Y and SHEP compared to parental SH-SY5Y

Fig. 5
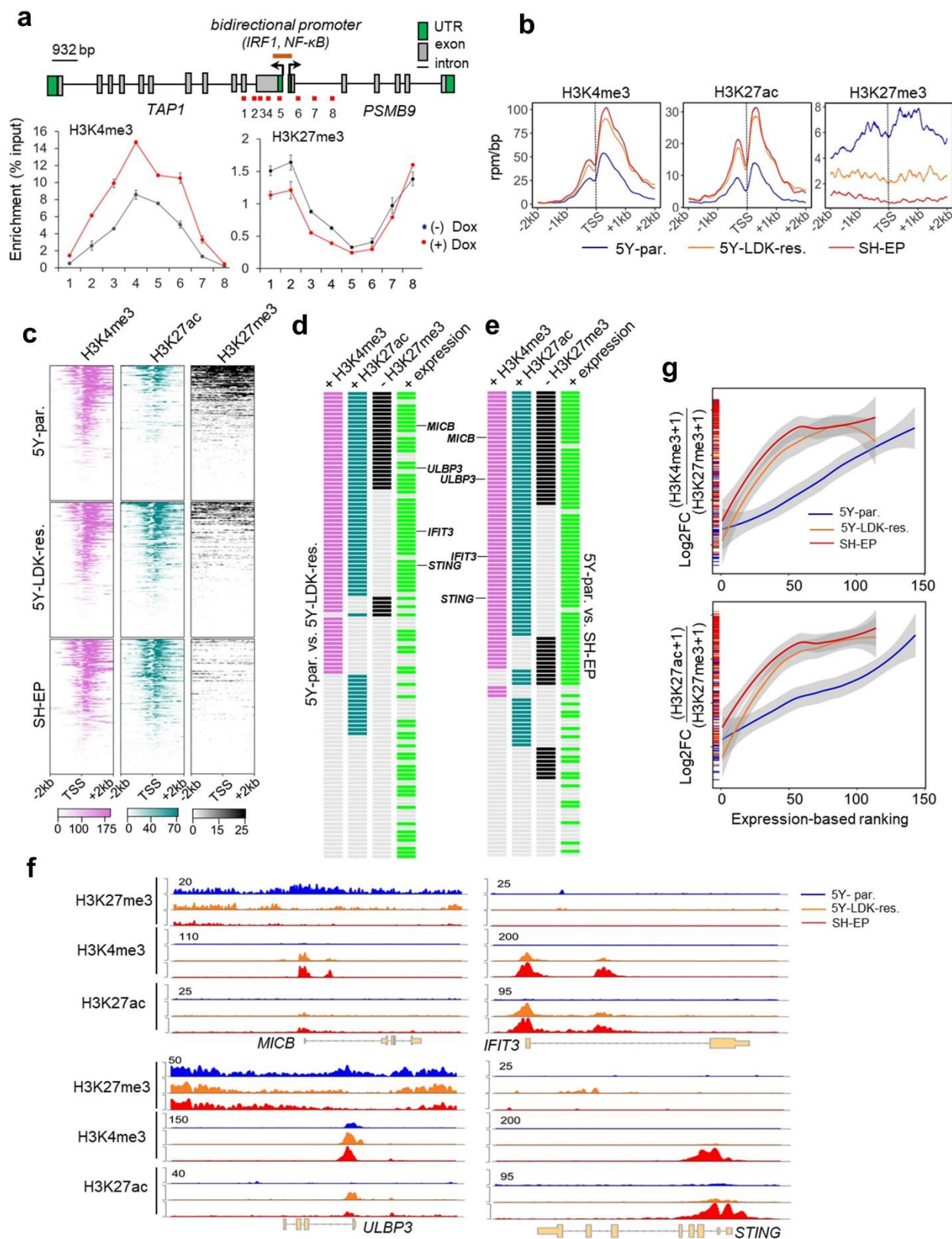
583   **Fig. 5. Activation o**f **immune gene expression associated with cell state transition is**

584   **epigenetically regulated. (a)** *Upper,* Linear representation of TAP1 and PSMB9 gene loci

585   showing the locations of the bidirectional promoter and IRF1 and NF-κB binding sites. The

586   amplicons (1-8) analyzed for histone mark occupancy are shown in red. *Lower,* ChIP-qPCR

587   analysis of H3K4me3 and H3K27me3 enrichment at the indicated amplicons along the

588   TAP1/PSMB9 locus in adrenergic SH-SY5Y cells expressing dox-inducible PRRX1 in the

589   presence or absence of dox (200 ng/mL) for 10 days. Data represent the means ± SD, n = 2

590   biological replicates. **(b)** Metagene representations of average ChIP-seq occupancies of the

591   indicated histone marks at the promoters of tumor cell-intrinsic immune response genes (TSS ±

592   2 kb; n = 134) in parental (5Y-par.), LDK-resistant (5Y-LDK-res.) SH-SY5Y and SH-EP NB cells.

593   **(c)** Heat map representation of histone enrichment at the same immune gene promoters as in

594   **(b)**, ranked in decreasing order of occupancy in the indicated cells. Each row represents the

595   normalized densities of histone marks within a ± 2 kb window centered on the TSS. **(d, e)**

596   Representation of pairwise comparisons between parental SH-SY5Y and LDK-resistant SH-SY5Y

597   **(d)**, and parental SH-SY5Y and SH-EP cells **(e).** The changes (+, gained; -, lost) in occupancies

598   of the active (H3K4me3, H3K27ac) and repressive (H3K27me3) histone marks ($\log_2$ FC ≥ 0.75,

599   TSS ± 2 kb), together with the corresponding changes in RNA expression (+, overexpressed; $\log_2$

600   FC ≥ 1) of each of the 134 tumor cell-intrinsic immune genes analyzed in **(b)** are shown.

601   Representative genes showing either a switch from repressive to active chromatin (*MICB, ULBP3*)

602   or associated only with a gain of active chromatin (*IFIT3, STING*) are shown. **(f)** ChIP-seq tracks

603   depicting the gain of active histone binding together with the loss of repressive histone binding

604   *(left)* or gain of active marks without changes in repressive mark occupancy *(right)* at the indicated

605   immune gene loci. Signal intensity is given at the top left corner for each track. **(g)** Loess

606   regression analysis of the correlation between the ratios of active to repressive histone binding at

607   the promoters (TSS ± 2kb) of immune response genes and their RNA expression (*Upper,*

608   H3K4me3:H3K27me3; *Lower*, H3K27ac:H3K27me3). Genes are ranked based on increasing

609   expression. Shaded regions represent 95% confidence intervals.

Supplementary Fig. 7.
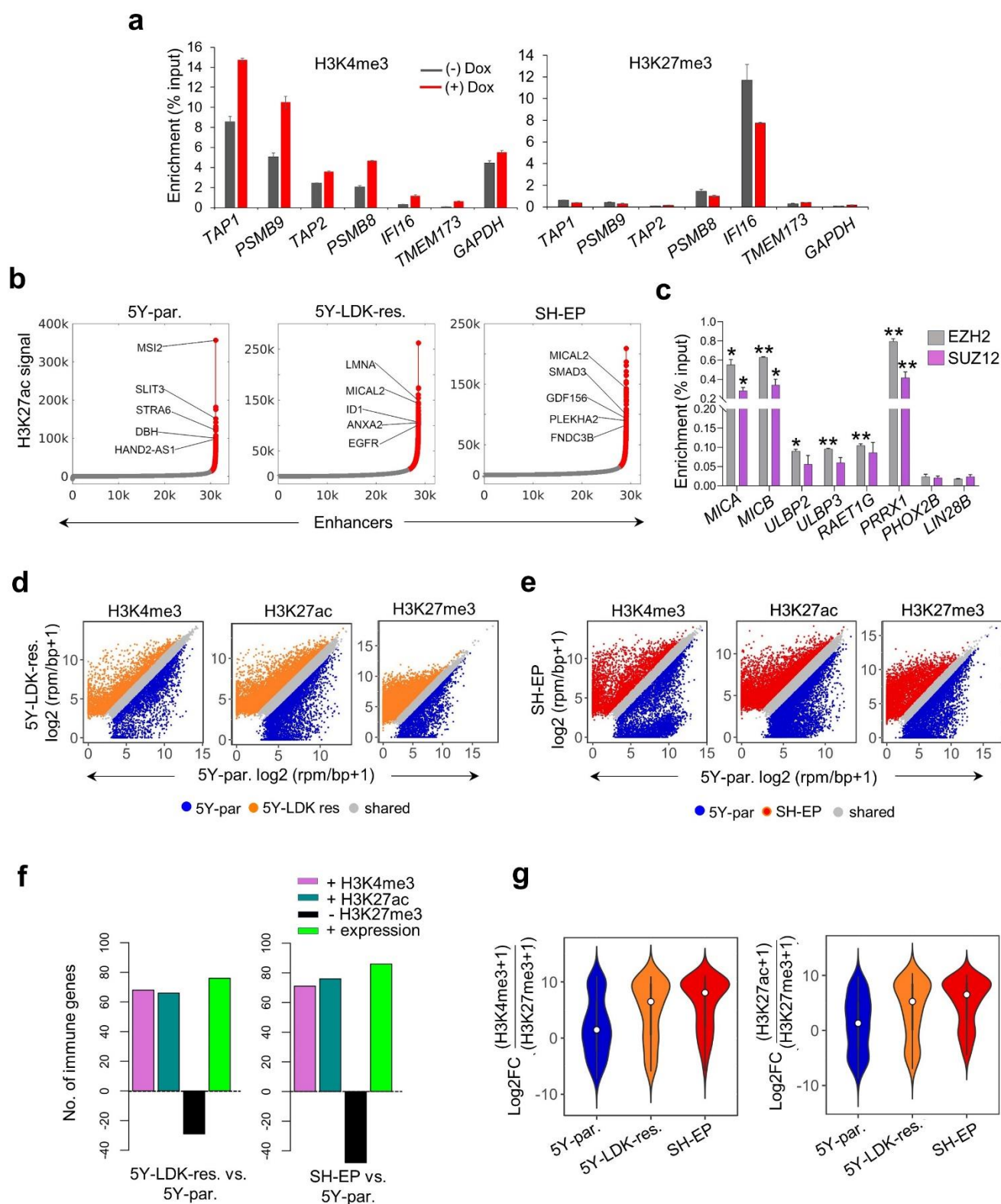
611　**Supplementary Fig. 7. Immune gene activation associated with the mesenchymal cell state**

612　**is epigenetically regulated. (a)** ChIP-qPCR analysis of H3K4me3 and H3K27me3 enrichment

613　at the promoters of the indicated immune genes in SH-SY5Y cells expressing doxycycline-

614　inducible PRRX1 in the presence or absence of dox (200 ng/mL) for 10 days**.** Enrichments at

615　TAP1 and PSMB9 loci correspond to amplicons 4 and 6 respectively, as described in **Fig. 5a**.

616　Data represent the means ± SD, n = 2 biological replicates. **(b)** Identification of enhancer regions

617　in parental SH-SY5Y, LDK-resistant SH-SY5Y and SH-EP cells. H3K27ac bound regions

618　identified as significant peaks were stitched together if they were within 12.5 kb of each other and

619　termed typical enhancers (plotted in grey). Super enhancers (SEs) were defined as stitched

620　enhancers surpassing the threshold signal based on the inclination point in all cell types (plotted

621　in red). In parental SH-SY5Y, LDK-resistant and SH-EP cells, 2.94% (915/31116), 6.56%

622　(1880/28635) and 4.18% (1215/29057) of the enhancers were classified as SEs respectively. The

623　top five SE-associated lineage-specific genes are highlighted. **(c)** ChIP-qPCR analysis of EZH2

624　and SUZ12 enrichment at the indicated genes in adrenergic 5Y-par. cells. Data represent the

625　means ± SD, n = 2 biological replicates, $^{*}P$ < 0.05; $^{**}P$ < 0.01 two-tailed Student's t-test. P-values

626　were calculated in comparison to enrichment observed at the Lin28B TSS (negative control

627　locus). **(d, e)** Scatter plots representing the differential binding of the indicated histone marks at

628　the promoter regions (TSS ± 2 kb) of all protein coding genes between parental SH-SY5Y (5Y-

629　par.) and LDK-resistant SH-SY5Y (5Y-LDK res.) **(d)**, and parental SH-SY5Y and SH-EP cells **(e)**.

630　rpm/bp, reads per million mapped reads per base pair. A ≥ 0.75 $\log_2$FC threshold was used to

631　identify unique peaks for each individual histone mark. Unique and shared peaks are shown in

632　different colors. **(f)** Bar plots representing the numbers of immune genes with increased

633　deposition of H3K4me3 and H3K27ac ($\log_2$ FC ≥ 0.75, TSS ± 2 kb) and loss of H3K27me3 ($\log_2$

634　FC ≥ 0.75, TSS ± 2 kb) histone marks, together with increased RNA expression ($\log_2$ FC ≥ 1) in

635　mesenchymal LDK-resistant SH-SY5Y (*left*) or SH-EP (*right*) as compared to adrenergic parental

636　SH-SY5Y cells. **(g)** Violin plots of the ratios of active to repressive histone marks (*left*,

42

637   H3K4me3:H3K27me3; *right*, H3K27ac:H3K27me3) surrounding immune gene promoters (TSS ±

638   2kb) in parental SH-SY5Y, LDK-resistant SH-SY5Y and SH-EP cells. Significance was

639   determined by the two-sided Wilcoxon rank-sum test.

640 cells **(Fig. 5b, c)**. On the other hand, the adrenergic parental SH-SY5Y cells showed significantly

641 higher occupancies of the H3K27me3 repressor mark at these immune gene promoters **(Fig. 5b,**

642 **c)**. Analysis of the polycomb repressive complex 2 (PRC2) that promotes H3K27me3 deposition

643 at repressed chromatin[50] revealed that immune response genes enriched for H3K27me3 binding,

644 such as those encoding the NKG2D ligands *MICA/B, ULBP2/3* and *RAET1G* had significantly

645 higher occupancies for PRC2 subunits, EZH2 and SUZ12 in adrenergic parental SH-SY5Y cells

646 compared to negative control regions that lacked H3K27me3 binding (*PHOX2B* and *LIN28B*)

647 **(Supplementary Fig. 7c)**, suggesting active immune gene repression in these cells.

648

649 We next sought to understand whether the activation of immune response genes observed

650 during the cell state transition from sensitivity to resistance represented a *switch* from repressive

651 to active chromatin or a *gain* of active chromatin marks. To this end, we quantified the changes

652 in histone binding occupancies between adrenergic parental SH-SY5Y and mesenchymal LDK-

653 resistant SH-SY5Y or SH-EP cells using pair-wise comparisons **(Supplementary Fig. 7d, e)**.

654 Compared to parental SH-SY5Y, LDK-resistant SH-SY5Y and SH-EP cells gained significant

655 H3K4me3 binding at the promoters of 60% and 62% immune genes (68 and 71 of 114)

656 respectively, which corresponded with their increased expression **(Fig. 5d, e; Supplementary**

657 **Fig. 7f).** A similar significant enrichment of the H3K27ac histone mark was observed at the

658 promoters of these immune genes [LDK-resistant SH-SY5Y, 58% (66/114); SH-EP, 67%

659 (76/114)]. Interestingly, gain of these active marks was accompanied by a concomitant loss of

660 H3K27me3 repressive histone binding at the promoters of 25% and 35% of (29 and 40 of 114)

661 immune genes in LDK-resistant SH-SY5Y and SH-EP cells respectively, as represented by the

662 NKG2D ligands, *MICB* and *ULBP3* **(Fig. 5d-f; Supplementary Fig. 7f).** On the other hand, in

663 LDK-resistant SH-SY5Y and SH-EP mesenchymal cells, 48% and 41% (55 and 47 of 114)

664 immune genes, such as the IFN-regulated factors *IFIT3 and STING,* gained either one or both

665 active marks without changes in occupancy of the repressive mark **(Fig. 5d-f; Supplementary**

666   **Fig. 7f)**. Furthermore, the mesenchymal cells showed a significantly higher ratio of active to

667   repressor histone binding at the TSSs of immune-related genes (H3K4me3 or

668   H3K27ac/H3K27me3) **(Supplementary Fig. 7g)**, which importantly, also correlated with the

669   increased expression of these genes in this cell state **(Fig. 5g)**. Therefore, our results suggest

670   that the immune gene activation observed with the transition from the adrenergic to the

671   mesenchymal cell state represents either a switch from repressive to active chromatin or a gain

672   of active chromatin at promoter regions.

673

674   **Mesenchymal neuroblastoma cells functionally engage cytotoxic T cells**

675   To assess the functional consequences of the increased immunogenicity associated with a

676   mesenchymal phenotype, we utilized the murine neuroblastoma cell line NB-9464, which was

677   derived from tumors arising in the Th-MYCN genetically engineered mouse model (GEMM). This

678   model was generated in immunocompetent C57BL/6 mice and the tumors recapitulate the genetic

679   and immunological features of human neuroblastoma[51,52]. We observed that NB-9464 cells

680   consisted of distinct populations that could be sorted on the basis of surface MHC class I H-2Kb

681   expression into high (H-2Kb^{hi})- or low (H-2Kb^{lo})-expressing populations **(Supplementary Fig. 8a;**

682   **Fig. 6a)**, both of which expressed transgenic human MYCN **(Fig. 6b)**. Consistent with our

683   hypothesis, H-2Kb^{hi} cells were enriched for *bona fide* mesenchymal markers - Prrx1, Sox9,

684   Notch1, and Snai2 (Slug) **(Fig. 6b)**, and showed enhanced migration and invasion, as might be

685   expected from their neural crest cell-like state **(Supplementary Fig. 8b, c)**. Importantly, the

686   mesenchymal H-2Kb^{hi} NB-9464 cells, but not their adrenergic H-2Kb^{lo} counterparts showed

687   augmented expression of cell surface class I MHC H-2Kb in response to IFN-γ, suggesting that

688   the mesenchymal cells had the potential for inducing a T cell-driven antitumor immune response

689   **(Fig. 6c)**.

690   Hence, to determine whether the increased MHC class I expression of mesenchymal versus

691   adrenergic cells translated into T cell activation, we first asked whether mesenchymal H-2Kb[hi]

692   NB-9464 cells were capable of exogenous antigen presentation. Using the well-characterized

693   chicken ovalbumin-derived peptide (OVA$_{257-264}$ or SIINFEKL) antigen that binds to H-2Kb and can

694   be recognized by specific T cell receptors (TCRs) on CD8^{+} T cells[53], we found that in comparison

695   to H-2Kb^{lo} cells, H-2Kb^{hi} cells expressed significantly higher levels of the H-2Kb-SIINFEKL

696   complex **(Fig. 6d)**. Next, we determined whether antigen presentation through H-2Kb enables

697   mesenchymal tumor cells to be recognized by antigen-specific T cell receptors (TCRs) on CD8^{+}

698   T cells, the first step towards a cytotoxic response. For this purpose, we used OT-I CD8^{+} T cells

699   from C57BL/6 mice expressing a transgenic TCR that specifically recognizes the H-2Kb-

700   SIINFEKL complex[53]. H-2Kb^{hi} or H-2Kb^{lo} cells loaded with the SIINFEKL peptide were cocultured

701   with naïve OT-I cells, after which OT-I activation was measured through cell surface CD69

702   expression, an early marker of T-cell activation[54]. Mesenchymal H-2Kb^{hi} cells led to significantly

703   higher OT-I activation in comparison with adrenergic H-2Kb^{lo} cells, indicating specific recognition

704   of the H-2Kb-SIINFEKL complex by the TCR on OT-I cells **(Fig. 6e)**. By contrast, co-cultures of

705   OT-I cells and either H-2Kb[lo] or H-2Kb[hi] NB-9464 neuroblastoma cells without the SIINFEKL

706   peptide did not lead to T-cell recognition, confirming the specificity of the TCR-antigen interaction

707   **(Fig. 6e)**. Finally, we investigated whether the differential MHC-I expression between adrenergic

708   and mesenchymal neuroblastoma cells influenced tumor growth *in vivo* through subcutaneous

709   injection of H-2Kb[hi] or H-2Kb^{lo} cells into syngeneic C57BL/6 (H-2Kb haplotype) mice

710   **(Supplementary Fig. 8d).** We noted an earlier onset of tumor formation with H-2Kb^{lo} cells

711   compared to H-2Kb^{hi} cells **(Supplementary Fig. 8d)**. However, once consistent tumor growth

712   was established, growth or survival rates did not change substantially between the two groups

713   **(Supplementary Fig. 8e)**, despite the persistence of higher H-2Kb and Prrx1 expression in the

714   H-2Kb[hi] tumors compared with the H-2Kb[lo] tumors **(Supplementary Fig. 8f,g).** While both types

715   of tumor cells had MYCN expression, histologically, in keeping with their adrenergic phenotype

Fig. 6.
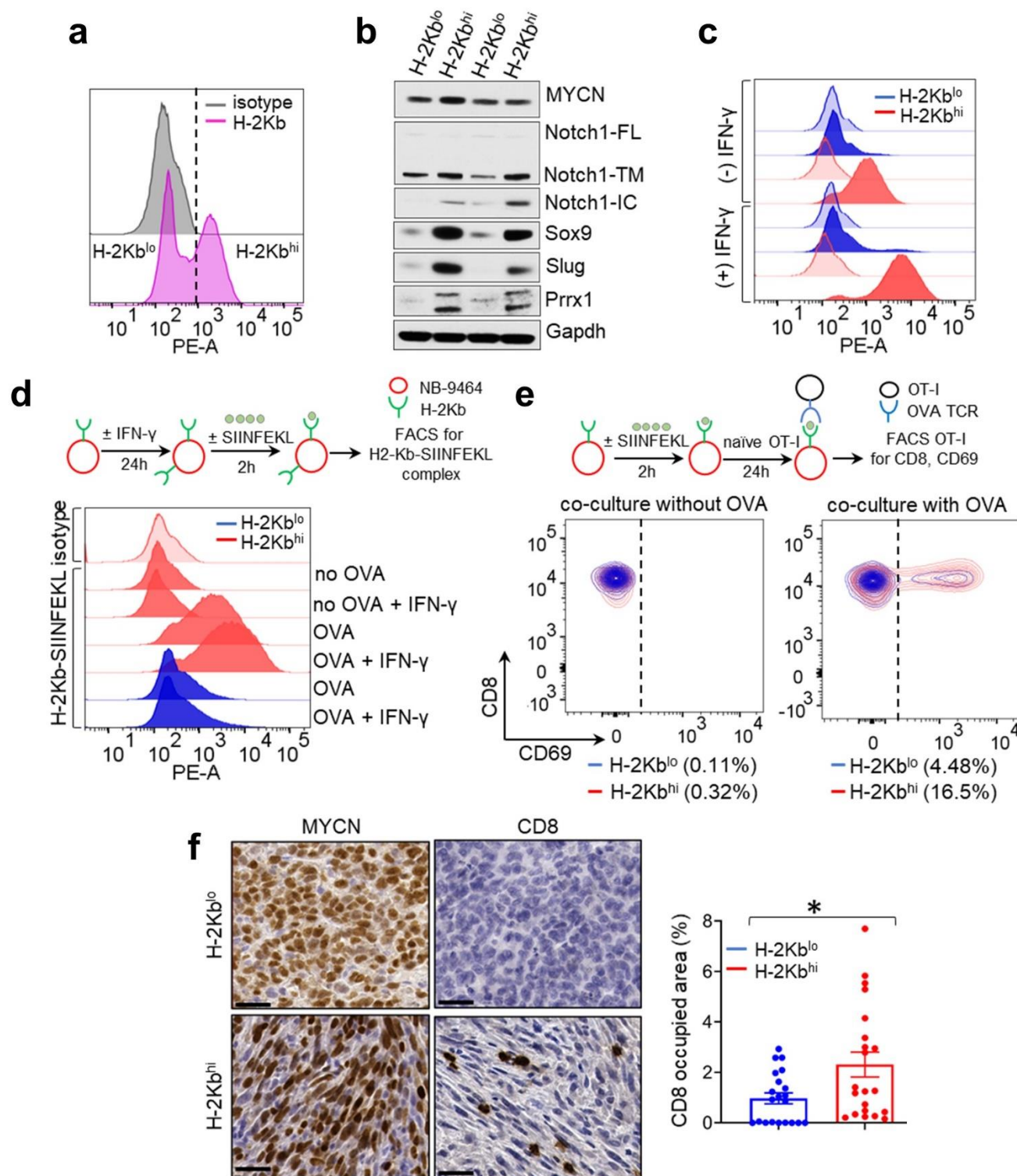
716 **Fig. 6. Mesenchymal NB cells functionally engage cytotoxic T cells. (a)** FACS analysis of

717 H-2Kb expression in unsorted NB-9464 cells. Vertical dashed line denotes the logscale

718 expression value used as a threshold to gate H-2Kb^{lo} and H-2Kb^{hi} cell populations. **(b)** WB

719 analysis of the indicated lineage markers in H-2Kb^{lo} and H-2Kb^{hi} cell populations. Notch1-FL, full

720 length; -TM, transmembrane; -IC, intracellular. GAPDH is used as a loading control. **(c)** FACS

721 analyses of basal and IFN-γ-induced (100 ng/mL for 24 hr.) surface H-2Kb expression (darker

722 colored histograms) in H-2Kb^{lo} and H-2Kb^{hi} cells compared to isotype controls (lighter colored

723 histograms). Plots representative of 2 independent experiments. **(d)** *Upper,* Schematic of OVA

724 binding assay. *Lower*, FACS analysis of surface H-2Kb-bound SIINFEKL OVA peptide in H-2Kb^{hi}

725 and H-2Kb^{lo} cells under basal or IFN-γ-induced conditions as in **(c)** and in the absence or

726 presence of the OVA peptide. Plots representative of 2 independent experiments. **(e)** *Upper,*

727 Schematic of NB-9464-OT-I co-culture assay. *Lower*, Contour plots showing the percentage of

728 naïve OT-I cells that were activated (CD8^{+} CD69^{+}) following co-culture with H-2Kb^{lo} and H-2Kb^{hi}

729 cells for 24 hr. with or without the OVA peptide. OT-I activation was measured by FACS analysis

730 of cell surface CD69. **(f)** *Left,* Immunohistochemical (IHC) staining for MYCN and CD8 expression

731 in representative murine NB xenograft tumors derived from NB-9464 H-2Kb^{lo} (adrenergic) and H-

732 2Kb^{hi} (mesenchymal) cells in immunocompetent syngeneic (C57BL/6) mice. Scale bars, 100 μm.

733 *Right*, Bar graphs showing the percentage of area occupied by CD8^{+} T cells in H-2Kb^{lo} (0.9% ±

734 0.2%) vs. H-2Kb^{hi} (2.3% ± 0.5%) tumors; *$*P$ < 0.05, two-tailed Welch's t-test. Each dot represents

735 one of three independent measurements for each tumor. Data represent mean ± SEM.

Supplementary Fig. 8.
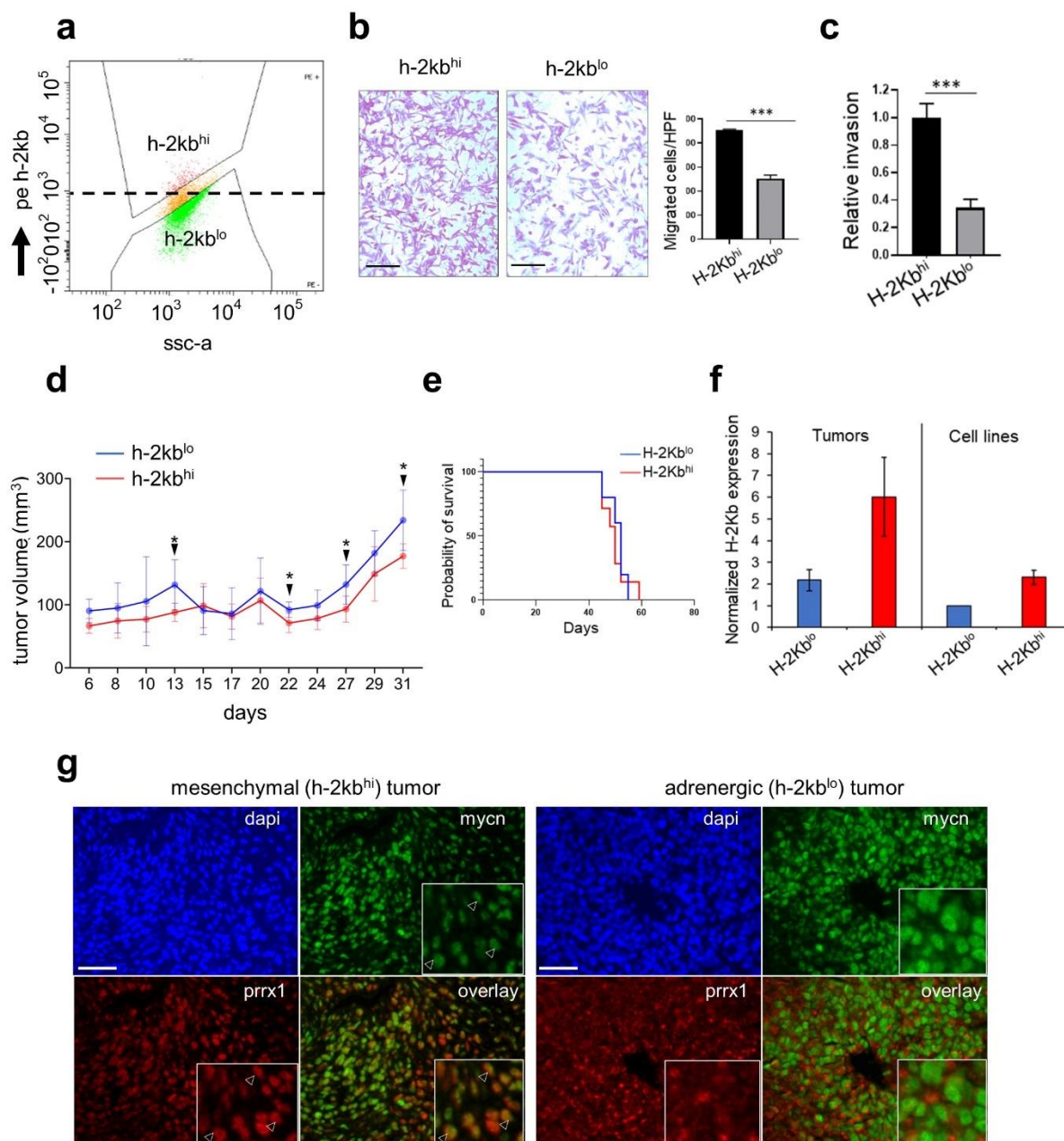
736 **Supplementary Fig. 8. Tumors that arise from NB-9464 H-2Kb^{hi} (mesenchymal) cells show**

737 **cytotoxic T cell infiltration**. **(a)** FACS scatter plot showing gating conditions used for sorting

738 NB-9464 cells into H-2Kb^{hi} and H-2Kb^{lo} populations. X axis represents side scatter (SSC-A); Y

739 axis denotes fluorescence intensity of surface H-2Kb detected using phycoerythrin (PE)-

740 conjugated antibody against H-2Kb. A logscale expression value of 10^3 was used as the threshold

741 (horizontal dashed line) to gate H-2Kb^{hi} ($\geq 10^3$) and H-2Kb^{lo} ($< 10^3$) populations. **(b)** *Left*, Bright

742 field images of crystal violet-stained H-2Kb^{hi} and H-2Kb^{lo} cells in transwell migration assays. Scale

743 bars, 100 µm. *Right,* Quantification of migrating cells per high-power field (HPF). Data represent

744 the means ± SD, *n* = 2 biological replicates, $^{***}P$ < 0.001; two-tailed Student's t-test. **(c)**

745 Quantification of the relative invasiveness of H-2Kb^{hi} and H-2Kb^{lo} cells. Data represent the means

746 ± SD, *n* = 2 biological replicates, $^{***}P$ < 0.001; two-tailed Student's t-test. **(d)** Tumor volumes in

747 immunocompetent C57BL/6 mice injected subcutaneously with 1 x 10^6 H-2Kb^{lo} or H-2Kb^{hi} NB-

748 9464 cells. Measurements were started on day 3 after injection and continued three times weekly

749 for up to 50 days or until euthanized due to tumor growth. Graphs represent changes in tumor

750 volume until day 31 (means ± SD; n = 7 per group at all time points) to highlight an earlier onset

751 of tumor formation with H-2Kb^{lo} cells compared to H-2Kb^{hi} cells. Tumors were considered to be

752 established upon reaching a volume of ~250 mm^3 (observed between days 31-34 for both H-2Kb^{lo}

753 and H-2Kb^{hi} tumors), following which both tumor types displayed equal increases in tumor growth

754 (data not shown). Tumor onset was defined as the day following which tumor volumes showed a

755 consistent increase (24.3 ± 2.2 days for H-2Kb^{lo} and 27.4 ± 2.1 days for H-2Kb^{hi} cells, *P* < 0.05).

756 Closed arrows refer to the indicated days (13, 22, 27 and 31) on which there were significant

757 differences in tumor volumes (day 13, *P* = 0.02; day 22, *P* = 0.01; day 27, *P* = 0.02 and day 31,

758 *P* = 0.02; *n* = 7 per group at all time points). All *P*-values calculated using the two-tailed Student's

759 t-test. **(e)** Kaplan-Meier survival analysis of immunocompetent C57BL/6 mice bearing NB tumor

760 xenografts derived from H-2Kb^{lo} (adrenergic) and H-2Kb^{hi} (mesenchymal) cells (50.8 ± 3.7 vs.

761 49.8 ± 4.8 days; *P* = 0.7; n = 7 per group; log-rank test. **(f)** RT-qPCR analysis of H-2Kb expression

762   in H-2Kb^{lo} and H-2Kb^{hi} NB tumor xenografts and the cell lines used to generate the xenografts.

763   Data represent the means ± SD, *n* = 3 biological replicates. **(g)** Immunofluorescence images of

764   MYCN (green) and Prrx1 (red) expression in representative murine NB xenograft tumors derived

765   from NB-9464 H-2Kb^{hi} (mesenchymal) and H-2Kb^{lo} (adrenergic) cells in immunocompetent

766   syngeneic (C57BL/6) mice. Nuclei are counterstained with DAPI (blue). Insets depict cells with

767   nuclear co-staining of MYCN and Prrx1 (arrowheads) and are exclusively present in the H-2Kb^{hi}

768   mesenchymal tumor. Scale bars, 100 µm, insets 33.3 µm.

769 H-2Kb^{lo} tumors were composed of densely arranged small round blue cells, whereas H-2Kb^{hi}

770 tumors predominantly comprised elongated, spindle-like cells interspersed with clusters of small

771 round blue cells **(Fig. 6f)**. We next analyzed the immune status of these tumors, reasoning that

772 tumors arising from immunogenic H-2Kb^{hi} cells would be infiltrated by T cells. Indeed, H-2Kb^{hi}

773 tumors showed significantly higher CD8^{+} T cell infiltration compared with H-2Kb^{lo} tumors **(Fig. 6f)**.

774 Taken together, these results suggest that the immunogenic traits of mesenchymal

775 neuroblastoma cells translate into the recruitment of cytotoxic T cells into the tumor

776 microenvironment.

777

778 **Mesenchymal neuroblastoma cells induce NK cell degranulation**

779 We next analyzed the functional relevance of the increased expression of the NKG2D NK cell

780 receptor ligands (ULBP1-3, MICA, MICB) seen in mesenchymal neuroblastoma tumors

781 **(Supplementary Fig. 4c; Fig. 4i)**. Since the interaction of the receptor with its cognate ligands

782 on target cells is the first step towards a cytotoxic response **(Fig. 7a)**, we compared the ability of

783 adrenergic (parental SH-SY5Y) and mesenchymal (LDK-resistant SH-SY5Y and SH-EP) cells to

784 bind to the recombinant NKG2D receptor fusion protein in an *in vitro* binding assay. Both

785 mesenchymal cell types showed increased binding to the NKG2D receptor, in keeping with their

786 increased cell surface expression of the ULBP2/3/5/6, MICA and MICB ligands **(Fig. 7b)**. NK cell

787 cytotoxicity is mediated by granzyme proteases and the pore-forming protein perforin, which in

788 resting cells are stored in secretory lysosomes or lytic granules marked by lysosome-associated

789 membrane protein-1 (LAMP-1 or CD107a)[55]. Upon target recognition, NK cells undergo

790 degranulation, or exocytosis of the lytic granules, which is associated with relocation of the

791 CD107a antigen to the cell membrane. Using cell-surface CD107a as a specific marker of

792 degranulation, we measured degranulation of peripheral blood NK cells harvested from healthy

793 human donors in the presence of parental SH-SY5Y, LDK-resistant SH-SY5Y and SH-EP targets.

Fig. 7.
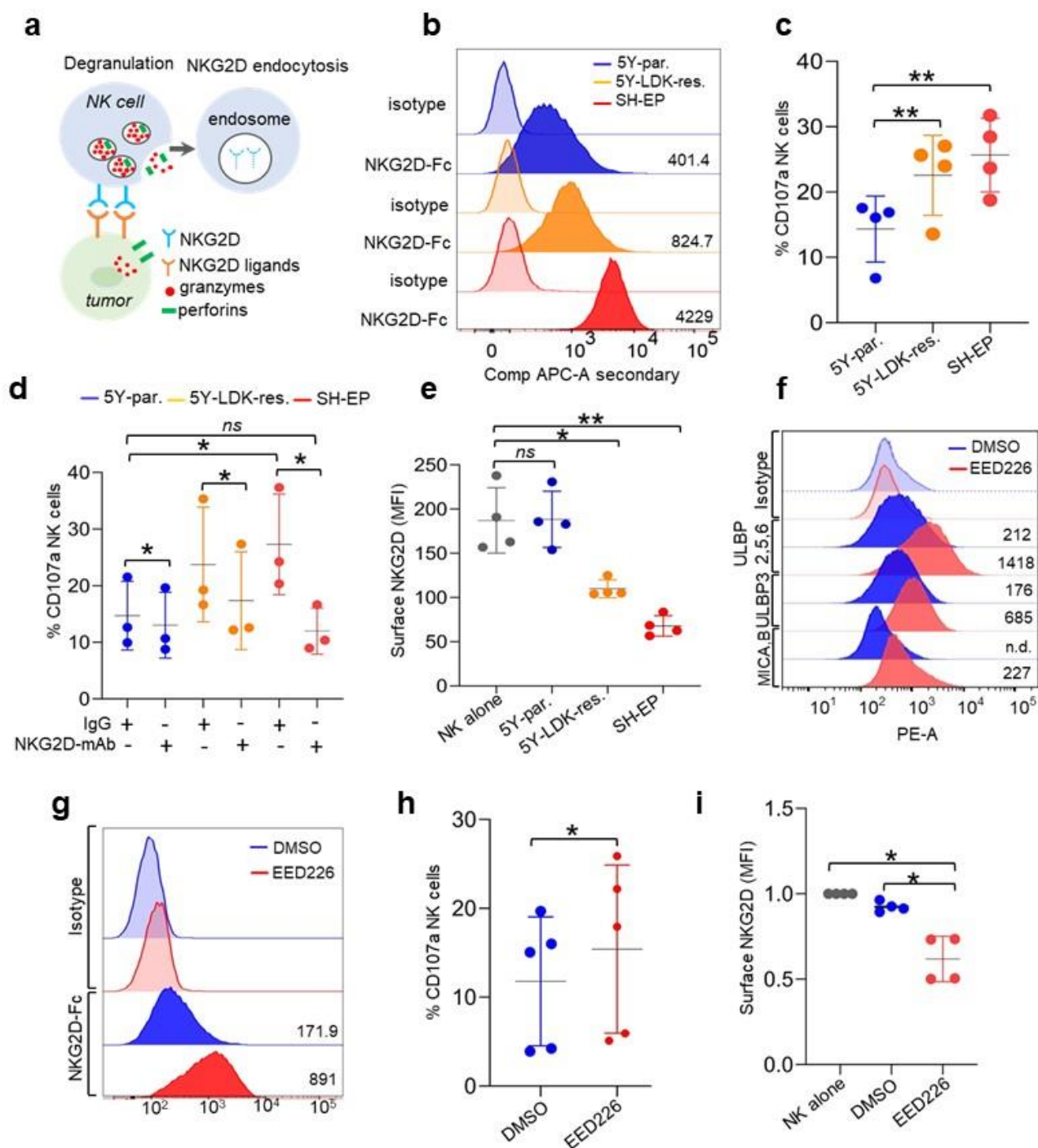
794 **Fig. 7. Mesenchymal NB cells induce NK cell degranulation. (a)** Schematic representation of

795 the interaction between NKG2D receptors on NK cells and cognate ligands on tumor cells, leading

796 to NK cell degranulation and receptor endocytosis. **(b)** FACS analysis of purified human NKG2D-

797 Fc protein binding (darker histograms) to adrenergic parental SH-SY5Y, and mesenchymal LDK-

798 resistant SH-SY5Y and SH-EP cells. Comp Alexa-647, compensated fluorescence intensity of

799 NKG2D-Fc protein detected using Alexa 647-conjugated anti-human IgG. Lighter histograms

800 indicate staining with Alexa 647-conjugated anti-human IgG only. Numbers indicate median

801 fluorescence intensity (MFI). Plots representative of 2 independent experiments. **(c)** X-Y plot

802 showing the percentage of degranulating NK cells following co-culture with the same cells as in

803 **(b)** for 4 hr. at an effector: target (E: T) cell ratio of 1:2. Degranulation was measured by FACS

804 analysis of cell-surface CD107a. Data represent the means ± SD, $n = 4$ biological replicates. **(d)**

805 X-Y plot showing the effect of a control IgG1 or an NKG2D blocking antibody on NK cell

806 degranulation following co-culture with the indicated cells for 4 hr. NK cell degranulation was

807 measured as in **(c).** Data represent the means ± SD, $n = 4$ biological replicates. **(e)** X-Y plot

808 depicting the MFI of NKG2D expression measured by FACS on naïve NK cells (NK alone) or

809 following co-culture with parental SH-SY5Y, LDK-resistant SH-SY5Y and SH-EP cells for 4 h.

810 Data represent the means ± SD, $n = 4$ biological replicates. **(f)** FACS analysis of surface

811 ULBP2/5/6, ULBP3, and MICA/MICB in adrenergic parental SH-SY5Y cells treated with DMSO

812 (vehicle control) or EED226 (5 μM for 8 days). **(g)** FACS analysis of purified human NKG2D-Fc

813 protein binding to parental SH-SY5Y cells treated with either DMSO or EED226 as in **(f)**. Light

814 gray histograms indicate human IgG1 isotype control. Numbers on the right represent MFI values

815 for FACS plots. Plots in **(f)** and **(g)** are representative of 2 independent experiments. **(h, i)** X-Y

816 plots showing NK cell degranulation **(h)** and MFI of surface-NKG2D **(i)** following co-culture of

817 naïve NK cells with parental SH-SY5Y cells treated with DMSO or EED226 as in **(f)**. NK cell

818 granulation and NKG2D MFI were measured as in **(c)** and **(e)**. Data represent means ± SD, $n =$

819   4 **(h)** and 5 **(i)** biological replicates. Significance for all results was calculated using the paired

820   two-tailed Student's t-test (*$P < 0.05$; **$P < 0.01$); *ns*, not significant

Supplementary Fig. 9.
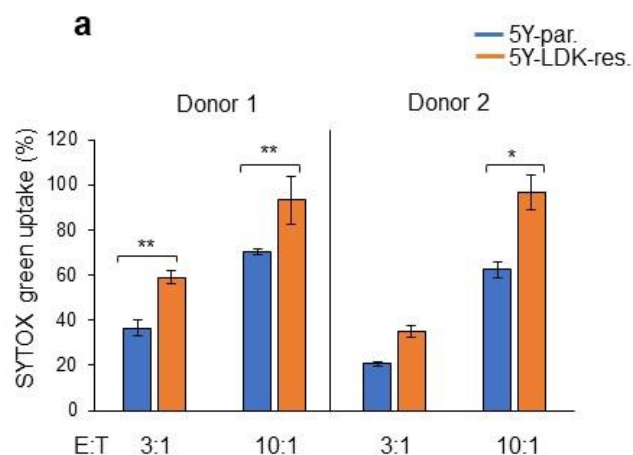
Supplementary Fig. 9. LDK-resistant SH-SY5Y cells are more susceptible to NK-induced cell death.

(a) Bargraphs showing NK-induced cell death in parental SH-SY5Y and LDK-resistant SH-SY5Y cells assessed by SYTOX green uptake following 1 hour of co-culture at indicated effector-to-target (E:T) ratios. Experiments were performed in two biological replicates using NK cells harvested from two independent donors. Data represent means ± SD, n = 3 technical replicates. Significance for all results was calculated using the paired two-tailed Student's t-test (*P < 0.05; **P < 0.01).

821   Co-culture of NK cells with LDK-resistant SH-SY5Y and SH-EP cells, both of which express

822   ligands for the NKG2D receptor, resulted in increased NK cell degranulation compared to parental

823   SH-SY5Y cells that did not express these ligands (**Fig. 7c**). To confirm that the increased NK cell

824   degranulation in LDK-resistant SH-SY5Y and SH-EP cells was specific to the NKG2D receptor,

825   we blocked its function with an anti-NKG2D monoclonal antibody. Compared to the isotype

826   control, blockade of NKG2D receptor activity completely abrogated the increased NK cell

827   degranulation in LDK-resistant SH-SY5Y and SH-EP cells, but had no effects on parental SH-

828   SY5Y cells, signifying that the modest but robust increase in degranulation in the presence of

829   mesenchymal cells was specific to the NKG2D receptor on NK cells **(Fig. 7d).** Upon interaction

830   with their cognate ligands on target cells, NKG2D receptors are internalized via ubiquitin-

831   dependent endocytosis leading to their lysosomal degradation, rendering the loss of surface

832   NKG2D receptor expression a robust readout for ligand-receptor engagement[56] **(Fig. 7a)**. In line

833   with the presence of functional NKG2D ligands on mesenchymal cells, co-cultures with LDK-

834   resistant SH-SY5Y and SH-EP cells led to significant downregulation of NK cell surface-

835   associated NKG2D expression, whereas co-culture with the adrenergic parental SH-SY5Y cells

836   did not alter the abundance of surface NKG2D expression **(Fig. 7e)**. Moreover, consistent with

837   the increased levels of NK degranulation upon co-culture with mesenchymal cells, LDK-resistant

838   SH-SY5Y were more susceptible to NK-induced cell death compared to parental SH-SY5Y cells

839   **(Supplementary Fig. 9a)**

840

841   The observation that genes encoding NKG2D ligands are repressed by the PRC2 complex in

842   adrenergic parental SH-SY5Y cells **(Supplementary Fig. 7c)** prompted us to examine whether

843   PRC2 inhibitors could induce the expression of these transcripts and influence NK cell function.

844   Indeed, treatment of parental SH-SY5Y cells with EED226, an allosteric inhibitor of the PRC2

845   complex[57], led to increased expression and surface localization of ULBP2/3 and MICA/B NKG2D

846   ligands **(Fig. 7f)**. Moreover, such increased ligand expression led to their increased binding to the

847   NKG2D receptor fusion protein in EED226-treated cells compared to cells treated with DMSO

848   alone **(Fig. 7g)**. Consequently, PRC2 inhibition resulted in an ~20% increase in NK cell

849   degranulation **(Fig. 7h)**. Finally, co-culture of primary NK cells with adrenergic parental SH-SY5Y

850   cells treated with EED226 led to a significant loss of surface NKG2D receptor expression **(Fig.**

851   **7i)**, suggesting that the increased degranulation resulting from PRC2 inhibition was driven by the

852   NKG2D receptor. Overall, these results suggest that the lineage-specific expression of NK cell

853   ligands in mesenchymal neuroblastoma cells has a functional impact on NK cell activity, and that

854   pretreatment of adrenergic neuroblastoma cells could potentially render these cells susceptible

855   to NK-cell mediated immunotherapy by upregulating ligand expression.

856 **DISCUSSION**

857 Despite the relatively poor track record of immunotherapy for neuroblastoma, growing evidence

858 suggests that subsets of these tumors have the potential to induce a productive immune

859 response[9]. Here, we demonstrate that the mesenchymal cell state, characterized by neural crest

860 cell (NCC)-like phenotypes, is a strong predictor of an antitumor immune response in

861 neuroblastoma. Induction of this state was accompanied by the expression of tumor cell-intrinsic

862 immune response-inducing genes that were epigenetically repressed in the more differentiated

863 (adrenergic) tumor cells. Importantly, inhibition of the PRC2 complex relieved such repression of

864 ligands for the activating NK cell receptor NKG2D, and led to NK cell degranulation, suggesting

865 that this strategy could be explored as a potential measure to improve the response of patients

866 with adrenergic neuroblastomas to NK cell-mediated therapy.

867

868 We sought to identify neuroblastomas capable of eliciting an immune response as those

869 characterized by the differential expression of immune gene signatures while remaining agnostic

870 to any of the established parameters that predict disease aggressiveness. Using UMAP

871 dimension reduction to analyze gene expression data from 498 primary neuroblastoma tumors,

872 we identified four clusters that were separated on the basis of differential activation of gene

873 networks that regulate the antitumor immune response, neuronal differentiation, MYCN-driven

874 processes and lipid metabolism. Intriguingly, the immunogenic cluster comprised almost equal

875 proportions of high- and low-risk tumors, raising the possibility that the molecular mechanisms

876 underlying immunogenicity in neuroblastoma are independent of disease aggressiveness. Thus,

877 our analysis using a cluster-based approach enabled the identification of antitumor immune

878 signatures as shared transcriptional programs between high- and low-risk neuroblastoma tumors,

879 a bridging feature that would have been missed in studies based solely on differential gene

880 expression between prognostically distinct groups of tumors.

881

882   A major finding of our study is the intimate link between tumor cell lineage and the propensity

883   of eliciting an immune response. Neuroblastoma tumors show lineage plasticity, underscored by

884   a phenotypic switch between undifferentiated NCC-like and more differentiated cells, two

885   divergent cell states driven by distinct transcriptional programs [37,38]. Our analysis revealed that

886   neuroblastomas enriched in NCC-derived signatures showed significantly higher antitumor

887   immunity featuring T and NK cells compared to tumors enriched for signatures of the adrenergic

888   lineage. Our finding is substantiated by studies showing that diverse cellular states such as

889   stemness, senescence and metastasis strongly influence the engagement of innate and adaptive

890   immune pathways [58-60]. Importantly, while the NCC-like/mesenchymal state promoted immune

891   response mechanisms such as upregulation of MHC class I and infiltration of cytotoxic

892   lymphocytes, these tumors were also characterized by the activation of immune checkpoints such

893   as regulatory T cells and exhaustion markers linked to immune suppression, similar to those

894   observed in chronic virally infected states [61]. The presence of such seemingly contradictory gene

895   signatures has important therapeutic implications for selecting patients who are likely to benefit

896   from T cell-based immunotherapies, as agents that target negative regulatory immune

897   checkpoints are likely to be most effective in those with a pre-existing but dampened antitumor

898   immune response [35]. Moreover, inhibition of cancer cell-intrinsic transcriptional programs that

899   promote T cell exclusion have been shown to effect changes in cell state and could potentially

900   employed to sensitize tumors to immunotherapy (Jerby-Arnon et al., 2018; Koyama et al., 2016;

901   Spranger et al., 2015).

902

903   In contrast to other *MYC*-driven cancers where high *MYC* levels restrain inflammatory

904   signaling and anti-tumor immune pathways[41,62], tumors within our immunogenic cluster, enriched

905   largely for mesenchymal/NCC signatures, had relatively high MYC expression that positively

906   correlated with immune cell infiltration. These diametrically opposite roles of MYC in regulating

907   immune response suggest that its transcriptional functions are likely to be very different in cancers

908   in which aberrant MYC expression is the main oncogenic driver compared to *MYCN*-nonamplified

909   neuroblastomas that are not dependent on MYC overexpression. This notion is supported by the

910   observation that inhibiting endogenous MYC function in non MYC-driven pancreatic cancer

911   models leads to decreased recruitment and retention of inflammatory cells[63]. As MYC is an

912   essential TF in NCCs[64,65], it is plausible that MYC promotes an immunogenic state by driving a

913   NCC-specific transcriptional program.

914

915   We also extended the analysis between cell state and immunogenicity to *MYCN*-amplified

916   tumors and identified a subset that incorporates both mesenchymal and immunogenic features.

917   This finding was substantiated by our data showing that expression of functional MHC class I is

918   retained in some *MYCN*-amplified mesenchymal neuroblastoma cells and is not perturbed by

919   changes in MYCN levels. Indeed, a robust antitumor immune response is observed during the

920   early stages of tumor development in Th-MYCN mice and in mouse-human chimeric tumors

921   derived from human NCCs expressing *MYCN* and oncogenic *ALK*[17]. Considering that these

922   mouse models are driven by gain of *MYCN* (~4-8 copies of the *MYCN* transgene)[17,52] rather than

923   the amplification seen in human tumors, and that absolute levels of MYCN protein dictate

924   transcriptional output[66], the relatively low MYCN dosage in these tumors may account for their

925   immunogenicity. These findings, if confirmed in additional data sets, should encourage us to

926   reconsider the notion that all *MYCN*-amplified tumors are intrinsically immune tolerant and that a

927   subset may in fact, be capable of inducing an immune response by virtue of their cell state.

928

929   The mutual exclusivity of the neuronal and immunogenic clusters suggests that

930   neuroblastomas with characteristics of neuronal differentiation (i.e. adrenergic phenotype) are

931   weakly immunogenic and thus incapable of inducing an effective immune response. Moreover,

932   the presence of NCC-derived gene expression signatures among immunogenic tumors indicates

933   that phenotypic reversal of sympathetic neuronal cells to an NCC-like state could contribute

934 significantly to the antitumor immune response. Such cell state-dependent immunogenic

935 switching could be mediated by the lineage-specific core regulatory circuitry (CRC) that drives

936 distinct transcriptomic states in neuroblastoma. Indeed, several TFs that constitute the NCC-like

937 (mesenchymal) CRC, including interferon regulatory factors 1-3 and IFI16, function as major

938 drivers of tumor cell-intrinsic innate and adaptive immune responses[67,68]. Furthermore, our data

939 identify PRRX1, another component of the mesenchymal CRC, as a regulator of MHC class I and

940 antigen-processing gene expression in neuroblastoma. Interestingly, PRRX1 was not identified

941 as a candidate regulator of MHC-I expression in genome-wide CRISPR knock-out screens to

942 identify NF-κB-dependent MHC-I suppressors in neuroblastoma[69], suggesting that the

943 mechanisms employed by PRRX1 could be independent of NF-kB activation and may involve

944 direct transcriptional activation of these genes. In addition, the upregulation of DNA damage

945 sensor proteins such as IFI16 and STING in mesenchymal neuroblastomas could also contribute

946 to the increased tumor-infiltrating lymphocyte abundance in these tumors, as suggested by results

947 in small cell lung cancer[70].

948

949   We have also established that the changes in immune gene expression accompanying the

950 adrenergic to mesenchymal transition are epigenetically regulated. Unlike lineage identity genes

951 that are regulated by super-enhancers, tumor cell-intrinsic immune genes involved in diverse

952 immune functions such as the inflammatory response, IFN-γ signaling and NK cell recognition,

953 are governed through changes in promoter structure, achieved by either *de novo* acquisition of

954 permissive chromatin or an epigenetic switch from PRC2-mediated repression to a permissive

955 chromatin landscape. Our findings support a role for the PRC2 complex in repressing genes that

956 encode ligands for the activating NK cell receptor NKG2D in adrenergic neuroblastoma cells and

957 the use of PRC2 inhibitors to augment the NK cell response against these cells. This approach is

958 justified on several grounds: our results add to the growing body of evidence for tumor-cell

959 autonomous function of PRC2 as a barrier to anti-tumor immunity, achieved through inhibition of

960   processes such as MHC expression[11,71], antigen processing and presentation and inflammatory

961   cytokine production[72,73]. Moreover, our observation that NKG2D ligands are enriched in

962   mesenchymal neuroblastomas coupled with the demonstration of the critical effector role of NK

963   cells in the antitumor immune response against this tumor [51] and the promising responses of

964   patients with other solid tumors to NKG2D-directed CAR NK cell therapy [74] strengthen this

965   premise. Considered together, the results of our analysis identify cell lineage as an important

966   determinant of the immune responsiveness of neuroblastoma and suggest rationales for the use

967   of immune-based therapies, either alone or in combination with epigenetic inhibitors, against the

968   two divergent phenotypes that define the lineage state of this pediatric tumor.

969

970

Acknowledgements

Author contributions

Sa.S. and R.E.G. conceived the study. Sa.S., A.C., B.C.M., J.L., and R.E.G. designed the experiments. Sa.S. performed the molecular, cellular and genomic studies. S.D. conceived and performed the genomic and computational analysis with inputs from R.D., Sa.S. and R.E.G. Sa.S., A.C., and B.C.M. performed the T and NK cell studies. B.S. performed the animal and cloning experiments. S.Z. performed quantitative analysis of IHC images. H.H. performed the cell migration assays. M.K., D.N.D., and L.S. contributed to FACS analysis, generation of LDK378-resistant SH-SY5Y cells, and compound testing, respectively. M.C., R.V., R.J., and St.S. contributed ideas towards regulation of immune function and cell lineage state. Sa.S., S.D., and R.E.G. wrote the manuscript with input from all authors.

Competing Interests

R.J. is a cofounder of Fate Therapeutics, Fulcrum Therapeutics, and Omega Therapeutics and an advisor to Dewpoint Therapeutics.

References

1. Yu, A.L. *et al.* Anti-GD2 antibody with GM-CSF, interleukin-2, and isotretinoin for neuroblastoma. *N Engl J Med* **363**, 1324-34 (2010).

2. Cheung, N.K. & Dyer, M.A. Neuroblastoma: developmental biology, cancer genomics and immunotherapy. *Nat Rev Cancer* **13**, 397-411 (2013).

3. Singh, N. *et al.* T cells targeting NY-ESO-1 demonstrate efficacy against disseminated neuroblastoma. *Oncoimmunology* **5**, e1040216 (2016).

4. Park, J.R. *et al.* Adoptive transfer of chimeric antigen receptor re-directed cytolytic T lymphocyte clones in patients with neuroblastoma. *Mol Ther* **15**, 825-33 (2007).

5. Pule, M.A. *et al.* Virus-specific T cells engineered to coexpress tumor-specific receptors: persistence and antitumor activity in individuals with neuroblastoma. *Nat Med* **14**, 1264-70 (2008).

6. Louis, C.U. *et al.* Antitumor activity and long-term fate of chimeric antigen receptor-positive T cells in patients with neuroblastoma. *Blood* **118**, 6050-6 (2011).

7. Merchant, M.S. *et al.* Phase I Clinical Trial of Ipilimumab in Pediatric Patients with Advanced Solid Tumors. *Clin Cancer Res* **22**, 1364-70 (2016).

8. Davis, K.L. *et al.* Nivolumab in children and young adults with relapsed or refractory solid tumours or lymphoma (ADVL1412): a multicentre, open-label, single-arm, phase 1-2 trial. *Lancet Oncol* **21**, 541-550 (2020).

9. Richards, R.M., Sotillo, E. & Majzner, R.G. CAR T Cell Therapy for Neuroblastoma. *Front Immunol* **9**, 2380 (2018).

10. Bernards, R., Dessain, S.K. & Weinberg, R.A. N-myc amplification causes down-modulation of MHC class I antigen expression in neuroblastoma. *Cell* **47**, 667-74 (1986).

11. Burr, M.L. *et al.* An Evolutionarily Conserved Function of Polycomb Silences the MHC Class I Antigen Presentation Pathway and Enables Immune Evasion in Cancer. *Cancer Cell* **36**, 385-401 e8 (2019).

12. Raffaghello, L. *et al.* Multiple defects of the antigen-processing machinery components in human neuroblastoma: immunotherapeutic implications. *Oncogene* **24**, 4634-44 (2005).

13. Raffaghello, L. *et al.* Downregulation and/or release of NKG2D ligands as immune evasion strategy of human neuroblastoma. *Neoplasia* **6**, 558-68 (2004).

14. Castriconi, R. *et al.* Identification of 4Ig-B7-H3 as a neuroblastoma-associated molecule that exerts a protective role from an NK cell-mediated lysis. *Proc Natl Acad Sci U S A* **101**, 12640-5 (2004).

15. Coughlin, C.M. *et al.* Immunosurveillance and survivin-specific T-cell immunity in children with high-risk neuroblastoma. *J Clin Oncol* **24**, 5725-34 (2006).

16. Betancur, P.A. *et al.* A CD47-associated super-enhancer links pro-inflammatory signalling to CD47 upregulation in breast cancer. *Nat Commun* **8**, 14802 (2017).

17. Cohen, M.A. *et al.* Formation of Human Neuroblastoma in Mouse-Human Neural Crest Chimeras. *Cell Stem Cell* **26**, 579-592 e6 (2020).

18. Asgharzadeh, S. *et al.* Clinical significance of tumor-associated inflammatory cells in metastatic neuroblastoma. *J Clin Oncol* **30**, 3525-32 (2012).

19. Song, L. *et al.* Valpha24-invariant NKT cells mediate antitumor activity via killing of tumor-associated macrophages. *J Clin Invest* **119**, 1524-36 (2009).

1049 20. Mao, Y. *et al.* Targeting Suppressive Myeloid Cells Potentiates Checkpoint Inhibitors to
1050 Control Spontaneous Neuroblastoma. *Clin Cancer Res* **22**, 3849-59 (2016).
1051 21. Tran, H.C. *et al.* TGFbetaR1 Blockade with Galunisertib (LY2157299) Enhances Anti-
1052 Neuroblastoma Activity of the Anti-GD2 Antibody Dinutuximab (ch14.18) with Natural
1053 Killer Cells. *Clin Cancer Res* **23**, 804-813 (2017).
1054 22. Brodeur, G.M., Seeger, R.C., Schwab, M., Varmus, H.E. & Bishop, J.M. Amplification of N-
1055 myc in untreated human neuroblastomas correlates with advanced disease stage. *Science*
1056 **224**, 1121-4 (1984).
1057 23. Seeger, R.C. *et al.* Association of multiple copies of the N-myc oncogene with rapid
1058 progression of neuroblastomas. *N Engl J Med* **313**, 1111-6 (1985).
1059 24. Layer, J.P. *et al.* Amplification of N-Myc is associated with a T-cell-poor microenvironment
1060 in metastatic neuroblastoma restraining interferon pathway activity and chemokine
1061 expression. *Oncoimmunology* **6**, e1320626 (2017).
1062 25. Wei, J.S. *et al.* Clinically Relevant Cytotoxic Immune Cell Signatures and Clonal Expansion
1063 of T-Cell Receptors in High-Risk MYCN-Not-Amplified Human Neuroblastoma. *Clin Cancer*
1064 *Res* **24**, 5673-5684 (2018).
1065 26. Brandetti, E. *et al.* MYCN is an immunosuppressive oncogene dampening the expression
1066 of ligands for NK-cell-activating receptors in human high-risk neuroblastoma.
1067 *Oncoimmunology* **6**, e1316439 (2017).
1068 27. Valentijn, L.J. *et al.* Functional MYCN signature predicts outcome of neuroblastoma
1069 irrespective of MYCN amplification. *Proc Natl Acad Sci U S A* **109**, 19190-5 (2012).
1070 28. Durbin, B.P., Hardin, J.S., Hawkins, D.M. & Rocke, D.M. A variance-stabilizing
1071 transformation for gene-expression microarray data. *Bioinformatics* **18 Suppl 1**, S105-10
1072 (2002).
1073 29. Lin, S.M., Du, P., Huber, W. & Kibbe, W.A. Model-based variance-stabilizing
1074 transformation for Illumina microarray data. *Nucleic Acids Res* **36**, e11 (2008).
1075 30. McInnes L, H.J. UMAP: Uniform manifold approximation and projection for dimension
1076 reduction. *arXiv preprint arXiv:1802.03426.* (2018).
1077 31. Becht, E. *et al.* Dimensionality reduction for visualizing single-cell data using UMAP. *Nat*
1078 *Biotechnol* (2018).
1079 32. Brodeur, G.M. *et al.* Revisions of the international criteria for neuroblastoma diagnosis,
1080 staging, and response to treatment. *Journal of Clinical Oncology* **11**, 1466-1477 (1993).
1081 33. Cohn, S.L. *et al.* The International Neuroblastoma Risk Group (INRG) classification system:
1082 an INRG Task Force report. *J Clin Oncol* **27**, 289-97 (2009).
1083 34. Satija, R., Farrell, J.A., Gennert, D., Schier, A.F. & Regev, A. Spatial reconstruction of single-
1084 cell gene expression data. *Nat Biotechnol* **33**, 495-502 (2015).
1085 35. Spranger, S. *et al.* Up-regulation of PD-L1, IDO, and T(regs) in the melanoma tumor
1086 microenvironment is driven by CD8(+) T cells. *Sci Transl Med* **5**, 200ra116 (2013).
1087 36. Wherry, E.J. & Kurachi, M. Molecular and cellular insights into T cell exhaustion. *Nat Rev*
1088 *Immunol* **15**, 486-99 (2015).
1089 37. Boeva, V. *et al.* Heterogeneity of neuroblastoma cell identity defined by transcriptional
1090 circuitries. *Nat Genet* **49**, 1408-1413 (2017).
1091 38. van Groningen, T. *et al.* Neuroblastoma is composed of two super-enhancer-associated
1092 differentiation states. *Nat Genet* **49**, 1261-1266 (2017).

1093   39.   Bindea, G. *et al.* Spatiotemporal dynamics of intratumoral immune cells reveal the
1094   immune landscape in human cancer. *Immunity* **39**, 782-95 (2013).
1095   40.   Wang, L.L. *et al.* Augmented expression of MYC and/or MYCN protein defines highly
1096   aggressive MYC-driven neuroblastoma: a Children's Oncology Group study. *Br J Cancer*
1097   **113**, 57-63 (2015).
1098   41.   Casey, S.C. *et al.* MYC regulates the antitumor immune response through CD47 and PD-
1099   L1. *Science* **352**, 227-31 (2016).
1100   42.   Cursons, J. *et al.* A Gene Signature Predicting Natural Killer Cell Infiltration and Improved
1101   Survival in Melanoma Patients. *Cancer Immunol Res* **7**, 1162-1174 (2019).
1102   43.   Newman, A.M. *et al.* Robust enumeration of cell subsets from tissue expression profiles.
1103   *Nat Methods* **12**, 453-7 (2015).
1104   44.   Hu, X. *et al.* Landscape of B cell immunity and related immune evasion in human cancers.
1105   *Nat Genet* **51**, 560-567 (2019).
1106   45.   Ross, R.A., Spengler, B.A. & Biedler, J.L. Coordinate morphological and biochemical
1107   interconversion of human neuroblastoma cells. *J Natl Cancer Inst* **71**, 741-7 (1983).
1108   46.   Cohn, S.L. *et al.* Prolonged N-myc protein half-life in a neuroblastoma cell line lacking N-
1109   myc amplification. *Oncogene* **5**, 1821-7 (1990).
1110   47.   Debruyne, D.N. *et al.* ALK inhibitor resistance in ALK(F1174L)-driven neuroblastoma is
1111   associated with AXL activation and induction of EMT. *Oncogene* **35**, 3681-91 (2016).
1112   48.   Chipumuro, E. *et al.* CDK7 inhibition suppresses super-enhancer-linked oncogenic
1113   transcription in MYCN-driven cancer. *Cell* **159**, 1126-1139 (2014).
1114   49.   Durbin, A.D. *et al.* Selective gene dependencies in MYCN-amplified neuroblastoma
1115   include the core transcriptional regulatory circuitry. *Nat Genet* **50**, 1240-1246 (2018).
1116   50.   Margueron, R. & Reinberg, D. The Polycomb complex PRC2 and its mark in life. *Nature*
1117   **469**, 343-9 (2011).
1118   51.   Kroesen, M. *et al.* A transplantable TH-MYCN transgenic tumor model in C57Bl/6 mice for
1119   preclinical immunological studies in neuroblastoma. *Int J Cancer* **134**, 1335-45 (2014).
1120   52.   Weiss, W.A., Aldape, K., Mohapatra, G., Feuerstein, B.G. & Bishop, J.M. Targeted
1121   expression of MYCN causes neuroblastoma in transgenic mice. *EMBO J* **16**, 2985-95
1122   (1997).
1123   53.   Clarke, S.R. *et al.* Characterization of the ovalbumin-specific TCR transgenic line OT-I: MHC
1124   elements for positive and negative selection. *Immunol Cell Biol* **78**, 110-7 (2000).
1125   54.   Cibrian, D. & Sanchez-Madrid, F. CD69: from activation marker to metabolic gatekeeper.
1126   *Eur J Immunol* **47**, 946-953 (2017).
1127   55.   Uhrberg, M. The CD107 mobilization assay: viable isolation and immunotherapeutic
1128   potential of tumor-cytolytic NK cells. *Leukemia* **19**, 707-9 (2005).
1129   56.   Molfetta, R. *et al.* Regulation of NKG2D Expression and Signaling by Endocytosis. *Trends
1130   Immunol* **37**, 790-802 (2016).
1131   57.   Qi, W. *et al.* An allosteric PRC2 inhibitor targeting the H3K27me3 binding pocket of EED.
1132   *Nat Chem Biol* **13**, 381-388 (2017).
1133   58.   Dongre, A. & Weinberg, R.A. New insights into the mechanisms of epithelial-mesenchymal
1134   transition and implications for cancer. *Nat Rev Mol Cell Biol* **20**, 69-84 (2019).
1135   59.   Malladi, S. *et al.* Metastatic Latency and Immune Evasion through Autocrine Inhibition of
1136   WNT. *Cell* **165**, 45-60 (2016).

1137   60.   Pereira, B.I. *et al.* Senescent cells evade immune clearance via HLA-E-mediated NK and
1138   CD8(+) T cell inhibition. *Nat Commun* **10**, 2387 (2019).
1139   61.   Shin, H. & Wherry, E.J. CD8 T cell dysfunction during chronic viral infection. *Curr Opin
1140   Immunol* **19**, 408-15 (2007).
1141   62.   Kortlever, R.M. *et al.* Myc Cooperates with Ras by Programming Inflammation and
1142   Immune Suppression. *Cell* **171**, 1301-1315 e14 (2017).
1143   63.   Sodir, N.M. *et al.* Endogenous Myc maintains the tumor microenvironment. *Genes Dev*
1144   **25**, 907-16 (2011).
1145   64.   Bellmeyer, A., Krase, J., Lindgren, J. & LaBonne, C. The protooncogene c-myc is an
1146   essential regulator of neural crest formation in xenopus. *Dev Cell* **4**, 827-39 (2003).
1147   65.   Rada-Iglesias, A. *et al.* Epigenomic annotation of enhancers predicts transcriptional
1148   regulators of human neural crest. *Cell Stem Cell* **11**, 633-48 (2012).
1149   66.   Zeid, R. *et al.* Enhancer invasion shapes MYCN-dependent transcriptional amplification in
1150   neuroblastoma. *Nat Genet* **50**, 515-523 (2018).
1151   67.   Chang, C.H., Hammer, J., Loh, J.E., Fodor, W.L. & Flavell, R.A. The activation of major
1152   histocompatibility complex class I genes by interferon regulatory factor-1 (IRF-1).
1153   *Immunogenetics* **35**, 378-84 (1992).
1154   68.   Unterholzner, L. *et al.* IFI16 is an innate immune sensor for intracellular DNA. *Nat
1155   Immunol* **11**, 997-1004 (2010).
1156   69.   Spel, L. *et al.* Nedd4-Binding Protein 1 and TNFAIP3-Interacting Protein 1 Control MHC-1
1157   Display in Neuroblastoma. *Cancer Res* **78**, 6621-6631 (2018).
1158   70.   Sen, T. *et al.* Targeting DNA Damage Response Promotes Antitumor Immunity through
1159   STING-Mediated T-cell Activation in Small Cell Lung Cancer. *Cancer Discov* **9**, 646-661
1160   (2019).
1161   71.   Ennishi, D. *et al.* Molecular and Genetic Characterization of MHC Deficiency Identifies
1162   EZH2 as Therapeutic Target for Enhancing Immune Recognition. *Cancer Discov* **9**, 546-563
1163   (2019).
1164   72.   Zingg, D. *et al.* The Histone Methyltransferase Ezh2 Controls Mechanisms of Adaptive
1165   Resistance to Tumor Immunotherapy. *Cell Rep* **20**, 854-867 (2017).
1166   73.   Peng, D. *et al.* Epigenetic silencing of TH1-type chemokines shapes tumour immunity and
1167   immunotherapy. *Nature* **527**, 249-53 (2015).
1168   74.   Xiao, L. *et al.* Adoptive Transfer of NKG2D CAR mRNA-Engineered Natural Killer Cells in
1169   Colorectal Cancer Patients. *Mol Ther* **27**, 1114-1125 (2019).
1170   75.   Schindelin, J. *et al.* Fiji: an open-source platform for biological-image analysis. *Nat
1171   Methods* **9**, 676-82 (2012).
1172   76.   Kamentsky, L. *et al.* Improved structure, function and compatibility for CellProfiler:
1173   modular high-throughput image analysis software. *Bioinformatics* **27**, 1179-80 (2011).
1174   77.   Love, M.I., Huber, W. & Anders, S. Moderated estimation of fold change and dispersion
1175   for RNA-seq data with DESeq2. *Genome Biol* **15**, 550 (2014).
1176   78.   Zhu, X. *et al.* Single-Cell Clustering Based on Shared Nearest Neighbor and Graph
1177   Partitioning. *Interdiscip Sci* **12**, 117-130 (2020).
1178   79.   Russo, P.S.T. *et al.* CEMiTool: a Bioconductor package for performing comprehensive
1179   modular co-expression analyses. *BMC Bioinformatics* **19**, 56 (2018).

1180   80.   Yu, G., Wang, L.G., Han, Y. & He, Q.Y. clusterProfiler: an R package for comparing biological
1181   themes among gene clusters. *OMICS* **16**, 284-7 (2012).
1182   81.   Alexopoulos, E.C. Introduction to multivariate regression analysis. *Hippokratia* **14**, 23-8
1183   (2010).
1184   82.   Das, S. & Bansal, M. Variation of gene expression in plants is influenced by gene
1185   architecture and structural properties of promoters. *PLoS One* **14**, e0212678 (2019).
1186   83.   Debruyne, D.N. *et al.* BORIS promotes chromatin regulatory interactions in treatment-
1187   resistant cancer cells. *Nature* **572**, 676-680 (2019).
1188

1189

1190 **Methods**

1191 **Cell culture**

1192 Human neuroblastoma (NB) cell lines (Kelly, NBL-S, CHP-212, SH-SY5Y, SH-EP, CHLA-20,

1193 NB69, SK-N-FI) were obtained from the Children's Oncology Group cell line bank. ACN, GI-ME-

1194 N, NB-EbC1 were kind gifts from A. Thomas Look and Kimberly Stegmaier at Dana Farber Cancer

1195 Institute (DFCI). NB-9464 cells were provided by To-Ha Thai at Beth Israel Deaconess Medical

1196 Center, Boston, MA. The cell lines were authenticated through STR analyses at the DFCI Core

1197 facility and were routinely tested for mycoplasma. All NB cells were grown in RPMI-1640 medium

1198 (Invitrogen) supplemented with 10% fetal bovine serum (FBS) (Invitrogen) and 1%

1199 penicillin/streptomycin (Life Technologies). HEK293T cells obtained from the American Type

1200 Culture Collection (ATCC) were grown in DMEM (Invitrogen) supplemented with 10% FBS and

1201 1% penicillin/streptomycin (Life Technologies). SH-SY5Y cells resistant to the ALK inhibitor

1202 ceritinib (LDK378) were described previously (Debruyne et al., 2016) and were grown in complete

1203 RPMI-1640 in the presence of 1.5 µM ceritinib.

1204

1205 **Generation of PRRX1-inducible cell lines**

1206 Lentiviral vectors containing wild type and DNA-binding mutants of PRRX1 were generated by

1207 cloning cDNAs encoding full length or homeodomain deletions of the human PRRX1A sequence

1208 into the pInducer20 lentiviral plasmid (gift from Stephen Elledge, Addgene plasmid #44012). The

1209 DNA-binding mutants harbor individual deletions of the three α-helices (ΔH1, ΔH2 and ΔH3) within

1210 the PRRX1 homeodomain (amino acids (aa) 94-153). Amino acid boundaries of the deleted

1211 regions are as follows: ΔH1 (aa 103-116); ΔH2 (aa 121-131); ΔH3 (aa 135-151). The lentivirus

1212 was packaged by co-transfection of pInducer20 plasmid with the helper plasmids, pCMV-

1213 deltaR8.91 and pMD2.G-VSV-G into HEK293T cells using the TransIT-LT1 Transfection Reagent

1214 (Mirus Bio LLC). Virus-containing supernatants were collected 48 hr after transfection. SH-SY5Y

1215 cells were transduced with the viral supernatant in the presence of 8 µg/ml polybrene (Sigma-

1216   Aldrich) and 24 hr later selected using neomycin (G418) (5 µg/ml). Induction of gene expression

1217   was achieved by treating cells every 2–3 days with doxycycline (dox; 200 ng/ml) in RPMI-1640

1218   medium supplemented with 10% tetracycline-negative fetal bovine serum (tet-free FBS) (Gemini

1219   Bio-Products) and 1% penicillin/streptomycin.

1220

1221   **MYCN shRNA knockdown and IFN-y treatment**

1222   The pLKO.1 shRNA construct targeting MYCN (TRCN0000020694) was purchased from Sigma-

1223   Aldrich and the pLKO.1 GFP shRNA was a gift from D. Sabatini (Addgene plasmid #30323).

1224   Lentiviral packaging was performed in HEK293T cells as decribed above and viral supernatant

1225   was collected on days 2 and 3 after transfection. Kelly human NB cells were transduced with the

1226   viral supernatant in the presence of 8 µg/ml polybrene (Sigma-Aldrich) and 24 h later selected

1227   using puromycin (1 µg/ml) for 2 days. Puromycin-resistant Kelly cells were cultured for an

1228   additional 6 days. Cells were then treated with 100 ng/ml of recombinant human IFNγ (Biolegend)

1229   for 24h, following which they were harvested for analysis of RNA and protein expression.

1230

1231   **FACS analysis for cell surface protein staining**

1232   For each staining reaction 1 x 10^6 live cells were placed in a 12 x 75 mm polystyrene round bottom

1233   tube (Falcon), resuspended in 100 µl 1x PBS and stained with the Zombie near-infrared (Zombie

1234   NIR) viability dye (BioLegend) at a 1:1,000 dilution for 15 minutes at RT. Cells were then washed

1235   once in FACS buffer (0.5% BSA in 1x PBS), resuspended in 100 µl of FACS buffer and incubated

1236   in 5 µl of Human TruStain FcX™ (Fc receptor blocking solution, BioLegend) for 10 minutes at RT.

1237   Next, appropriate volumes of conjugated fluorescent primary antibodies at predetermined

1238   optimum concentrations were added and incubated on ice for 20 minutes in the dark. Cells were

1239   then washed once in 2 ml of FACS buffer by centrifugation at 1500 rpm for 5 minutes. All FACS

1240   samples were analyzed on a FACSCalibur flow cytometer (Becton Dickinson) using Cell Quest

1241   software (Becton Dickinson). A minimum of 50,000 events was counted per sample and used for

1242 further analysis. Data were analyzed using FlowJo v10 software (Becton Dickinson). The following

1243 primary antibodies were used: PE-HLA (Biolegend; clone W6/32), PE-MICA/B (Biolegend clone

1244 6D4), PE-ULBP2 (R&D Systems; clone 165903), PE-ULBP3 (R&D Systems; clone 166510), PE-

1245 H-2Kb (Biolegend AF6-88.5), PE-H-2Kb SIINFEKL (Biolegend; clone 25-D1.16), PE-mouse

1246 IgG2a k isotype control (Biolegend MOPC-173), PE- mouse IgG1 k isotype control (MOPC-21).

1247

1248 **Cell viability assay**

1249 SH-SY5Y parental and SH-SY5Y LDK-resistant cells were seeded in 96-well plates at a density

1250 of 2×10^3 cells/well. After 24 h, cells were treated with increasing concentrations of LDK378

1251 (ranging from 1 nM to 10 µM) dissolved in Dimethyl Sulfoxide (DMSO). DMSO solvent without the

1252 drug served as a negative control. Following 72 h incubation, cells were analyzed for viability

1253 using the CellTiter-Glo Luminescent Cell Viability Assay (Promega) according to the

1254 manufacturer's instructions. Drug concentrations that inhibited cell growth by 50% (IC_{50}) were

1255 determined using a non-linear regression curve fit with GraphPad Prism 8 software.

1256

1257 **Cell migration and invasion assays**

1258 Cell migration was measured using transwell chambers (Falcon). NB9464-H-2Kb^{lo} or

1259 NB9464-H-2Kb^{hi} cells in serum-free medium (0.5 x 10^6 cells/ml) were added to the upper

1260 chamber and inserts (8 µm pore size) were placed in the lower chamber containing medium

1261 with 10% FBS. Following incubation at 37° C for 8 h, cells that migrated to the lower chamber

1262 were fixed with methanol and stained with crystal violet (Sigma-Aldrich). The stained cells

1263 were photographed with a light microscope at 100X magnification and migration was

1264 quantified as the number of cells per high power field. Cell invasion was measured using the

1265 fluorometric QCM™ ECMatrix™ Cell Invasion Assay (Millipore). NB9464-H-2Kb^{lo} or NB9464-

1266 H-2Kb^{hi} cells in serum-free medium (0.5 x 10^6 cells/ml) were added to the upper chamber

1267 and inserts (8 µm pore size) placed in the lower chamber containing medium with 10% FBS.

1268 Following incubation at 37° C for 24 h, cell invasion was measured according to

1269 manufacturer's instructions.

1270

1271 **EED226 treatment**

1272 5 x10^5 SH-SY5Y cells were seeded into 10 cm plates and treated with either 5 µM EED226

1273 (Selleck Chemicals) or DMSO (vehicle control) for 6-8 days, following which samples were

1274 harvested for downstream analyses. Cells were replenished with fresh media containing DMSO

1275 or EED226 every 2 days.

1276

1277 **Compounds**

1278 Ceritinib (LDK378) and EED226 were purchased from Selleck Chemicals. Doxycycline and

1279 dimethyl Sulfoxide (DMSO) was purchased from Sigma-Aldrich.

1280

1281 **RNA extraction and q-PCR**

1282 Total RNA was isolated using the RNAeasy Mini kit (Qiagen). Purified RNA was reverse

1283 transcribed to cDNA using Superscript IV VILO master mix (Thermo Fisher Scientific) following

1284 the manufacturer's protocol. Quantitative PCR was performed using 1 µl cDNA, 1x PowerTrack

1285 SYBR Green PCR master mix (Thermo Fisher Scientific) and PCR primers (200 nM) in a total

1286 volume of 25 µl and analyzed on a ViiA 7 Real-Time PCR system (Thermo Fisher Scientific). Each

1287 individual biological sample was amplified in technical duplicate and normalized to GAPDH as an

1288 internal control. Relative expression was calculated according to the $2^{-\Delta\Delta CT}$ quantification method

1289 (Livak and Schmittgen, 2001). PCR primer sequences are shown in Table S5.

1290

1291

1292

Synthetic RNA spike-in and RNA-sequencing

RNA-sequencing was performed on the following human NB cell lines: Kelly, NBL-S, CHP-212, SH-SY5Y, SH-SY5Y LDK-resistant and SH-EP. Biological duplicates (5 x 10^6 cells per replicate) were homogenized in 1 ml of TRIzol Reagent (Invitrogen) and purified using the mirVANA miRNA isolation kit (Ambion) following the manufacturer's instructions. Total RNA was treated with DNA-free^{TM} DNase I (Ambion), spiked-in with ERCC RNA Spike-In Mix (Ambion) and analyzed on an Agilent 2100 Bioanalyzer (Agilent Technologies) for integrity. Sequencing libraries were prepared using LP-KAPA mRNA Hyper Prep and sequenced using Illumina HiSeq for 40 bases.

Western blotting

Cells were homogenized in NP40 lysis buffer (Life Technologies) containing 1× cOmplete EDTA-free protease inhibitor cocktail and 1x PhosSTOP (Roche). Protein concentration was measured using the DC Protein Assay (Bio-Rad). 100 µg total protein was denatured in LDS sample buffer (Invitrogen), separated on pre-cast 4-12% Bis-Tris gels (Invitrogen) and transferred to nitrocellulose membranes (Bio-Rad). Membranes were blocked using 5% dry milk (Sigma-Aldrich) in Tris-buffered saline (TBS) supplemented with 0.2% Tween-20 (TBS-T) for 1 hr, and incubated overnight with primary antibody in blocking buffer at 4 °C. Chemiluminescent detection was performed with appropriate HRP-conjugated secondary antibodies and enhanced chemiluminescence reagents (Thermo Scientific). Images were developed using Genemate Blue ultra-autoradiography film (VWR).

Antibodies

The following primary antibodies were used: MYCN (Cat #51705), MYC (13987), GATA3 (5852), TAP1 (12341), TAP2 (12259), LMP7 (13635), NOTCH1 (3608), cleaved NOTCH1 (4147), SOX9 (82630), AXL (8661), GAPDH (2118), β-actin (3700), IRF1 (8478), VIM (5741), YAP1 (4912),

1318   TAZ1 (4883) (Cell Signalling Technologies (CST)); PHOX2B (Abcam;183741), FN1 (RnD

1319   systems; AF1918), LMP2 (Santa Cruz; 271354) and PRRX1 (Santa Cruz; 293386).

1320

Chromatin immunoprecipitation-quantitative PCR (ChIP-qPCR)

1322   Soluble chromatin was prepared as above from SH-SY5Y cells without or with dox-inducible

1323   PRRX1 expression (200 ng/ml dox for 10 days). ChIP was performed as described in the

1324   preceding section using the following antibodies: H3K4me3 (Abcam 8580), H3K27me3 (Millipore

1325   07-729), EZH2 (CST 5246), SUZ12 (CST 3737), EED (Millipore 17-10034), rabbit IgG (CST

1326   2729). Purified ChIP DNA was dissolved in 60 µl of 1x TE. Quantitative PCR was performed on a

1327   ViiA 7 Real-Time PCR system (Thermo Fisher Scientific) with 1 µl purified DNA, 1x PowerTrack

1328   SYBR Green PCR master mix (Thermo Fisher Scientific) and PCR primers (200 nM) against the

1329   genomic regions of interest. Each individual biological sample was amplified in technical

1330   duplicate. Relative enrichment was quantified using the percent input method. PCR primer

1331   sequences are shown in Table S5.

1332

Chromatin immunoprecipitation-sequencing (ChIP-seq)

1334   Approximately 10-12 x 10^7 cells were crosslinked with 1% formaldehyde (Thermo Scientific) for

1335   10 min at room temperature (RT) followed by quenching with 0.125 M glycine for 5 min. The cells

1336   were then washed twice in ice-cold 1x Phosphate Buffered Saline (PBS), and the cell pellet

1337   equivalent of 4 x 10^7 cells were flash frozen and stored at −80°C. Crosslinked cells were lysed in

1338   lysis buffer 1 (50 mM HEPES-KOH pH7.5, 140 mM NaCl, 1 mM EDTA, 10% glycerol, 0.5% NP40,

1339   0.25% Triton X-100). The resultant nuclear pellet was washed once in lysis buffer 2 (10 mM Tris-

1340   HCl pH 8, 200 mM NaCl, 1 mM EDTA, 0.5 mM EGTA) and then resuspended in sonication buffer

1341   (50 mM HEPES-KOH pH 7.5, 140 mM NaCl, 1mM EDTA, 1mM EGTA, 1% Triton X-100, 0.1%

1342   sodium deoxycholate, 0.2% SDS). Chromatin was sheared using a Misonix 3000 sonicator

1343   (Misonix) and at the following settings: 10 cycles, each for 30 s on, followed by 1 min off, at a

1344   power of approximately 20 W. The lysates were then centrifuged for 15 min at 4 °C, supernatants

1345   collected and diluted with an equal amount of sonication buffer without SDS to reach a final

1346   concentration of 0.1% SDS. For each ChIP, the chromatin equivalent of 1×10^7 cells was used.

1347   50 µl of Protein G Dynabeads per sample (Invitrogen) were blocked with 0.5% BSA (w/v) in 1x

1348   PBS. Magnetic beads were loaded with the following antibodies: 10 µg of H3K27me3 (Millipore

1349   07-729); 3 µg of H3K27ac (Abcam 4729), and 3 µg of H3K4me3 (Abcam 8580) and incubated

1350   overnight at 4°C. The sonicated lysates were then incubated overnight at 4°C with the antibody-

1351   bound magnetic beads, washed with low-salt buffer (50 mM HEPES-KOH (pH 7.5), 0.1% SDS,

1352   1% Triton X-100, 0.1% sodium deoxycholate, 1 mM EGTA, 1 mM EDTA, 140 mM NaCl and 1×

1353   complete protease inhibitor), high-salt buffer (50 mM HEPES-KOH (pH 7.5), 0.1% SDS, 1% Triton

1354   X-100, 0.1% sodium deoxycholate, 1 mM EGTA, 1 mM EDTA, 500 mM NaCl and 1× complete

1355   protease inhibitor), LiCl buffer (20 mM Tris-HCl (pH 8), 0.5% NP-40, 0.5% sodium deoxycholate,

1356   1 mM EDTA, 250 mM LiCl and 1× complete protease inhibitor) and Tris-EDTA (TE) buffer. DNA

1357   was then eluted in elution buffer (50 mM Tris-HCl (pH 8.0), 10 mM EDTA, 1% SDS), and high-

1358   speed centrifugation performed to pellet the magnetic beads and collect the supernatants. The

1359   crosslinking was reversed overnight at 65° C in the presence of 300 mM NaCl. RNA and protein

1360   were digested using RNase A and proteinase K, respectively, and DNA was purified with phenol-

1361   chloroform extraction and ethanol precipitation. Purified ChIP DNA was used to prepare Illumina

1362   multiplexed sequencing libraries using the NEBNext Ultra II DNA Library Prep kit and the

1363   NEBNext Multiplex Oligos for Illumina (New England Biolabs) according to the manufacturer's

1364   protocol. Libraries with distinct indices were multiplexed and run together on the Illumina NextSeq

1365   500 (SY-415-1001, Illumina) for 75 base pairs.

1366

1367   IFN-gamma induction and antigen presentation in NB9464 cells

1368   Approximately 1×10^6 cells were seeded onto 10 cm plates. 24 hr later, adherent cells were

1369   treated with recombinant mouse IFN-γ (Biolegend) for 24h and harvested for H-2Kb analysis

1370 using FACS as described above. For antigen presentation assays, cells treated with IFN-γ were

1371 pulsed with SIINFEKL (OVA peptide) at 37°C. Cells were subsequently washed with 1x PBS to

1372 remove unbound peptide and processed for analysis using FACS.

1373

1374 **T cell activation assays**

1375 OT-I T cell receptor (TCR) transgenic mice were purchased from Jackson Laboratories (Bar

1376 Harbor, ME). Splenocytes were harvested and T cells were subsequently isolated from the

1377 mononuclear layer using Ficoll separation and directly used in co-culture assays. Successful

1378 enrichment of CD8$^+$ T cells was confirmed by FACS analysis using the FITC-CD8 antibody. Cells

1379 were pulsed with SIINFEKL (OVA peptide) at 37 °C, to bind to cell surface H-2Kb. Cells were

1380 subsequently washed with 1x PBS to remove unbound peptide and then co-cultured with

1381 unstimulated OT-1 T cells for 24 h. OT-I cells were then harvested, and sequentially stained with

1382 the Zombie NIR viability dye and FITC-CD8, PE-CD69 antibodies, followed by fixation with 1%

1383 paraformaldehyde (Polysciences, Inc). OT-1 cells were analyzed by flow cytometry using a

1384 FACSCanto II cell analyzer (Becton Dickinson) and FlowJo V10 software (Becton Dickinson).

1385

1386 **In vitro assays for NKG2D binding**

1387 SH-SY5Y parental, SH-SY5Y LDK-resistant, and SH-EP cells were incubated with recombinant

1388 human NKG2D-Fc chimeric protein or an equivalent concentration of human IgG , following which

1389 cells were washed, and sequentially stained with the Zombie NIR viability dye as described above

1390 followed by incubation with an Alexa 647-conjugated anti-human IgG antibody for 30 minutes.

1391 Cells were washed in FACS buffer and analyzed by flow cytometry using a FACSCanto II cell

1392 analyzer (Becton Dickinson) and FlowJo V10 software (Becton Dickinson).

1393

1394

1395

1396 **NK cell degranulation assays**

1397 Human peripheral blood NK cells were isolated from blood collars using a RosetteSep™ human

1398 NK cell enrichment cocktail (STEMCELL Technologies). NK cells were then co-cultured for 4 h

1399 with confluent monolayers of SH-SY5Y parental, SH-SY5Y LDK-resistant, and SH-EP cells at in

1400 the presence of CD107a antibody (Biolegend). Additionally, co-cultures of NK cells and 721.221

1401 B cells were included as positive controls for degranulation. At the endpoint, NK cells were

1402 harvested, stained with Zombie Yellow (Biolegend) and CD56 FITC (or NKp46 AlexaFluor 647^{TM})

1403 and NKG2D PE (or mouse IgG1 PE) antibodies (Biolegend), followed by fixation with 1%

1404 paraformaldehyde (Polysciences, Inc). For the NKG2D blocking assay, NK cells were incubated

1405 with purified anti-NKG2D antibody or mouse IgG1 isotype control at 37 ℃, following which the

1406 degranulation assay was performed as detailed above. NK cells were analyzed by flow cytometry

1407 using a FACS Canto II (Becton Dickinson) and FlowJo V10 software (Becton Dickinson).

1408

1409 **Data sets**

1410 Publicly available RNA-seq data (GEO accession number GSE49711/GSE62564) from a cohort

1411 of 498 primary human neuroblastoma tumors, microarray expression data from 394

1412 neuroblastoma tumors (GSE120572) and 24 human neuroblastoma cell lines (GSE28019) were

1413 accessed through the R2 genomics analysis and visualization platform

1414 (https://hgserver1.amc.nl/cgi-bin/r2/). Clinical annotations for tumors were obtained from

1415 GSE49711/GSE62564 regarding MYCN status (MYCN-nonamplified vs. MYCN-amplified, INSS

1416 stage [high (stage 4) vs. low (1, 2, 3 and 4s], risk status (high vs. low) and age (< 18 months vs.

1417 ≥ 18 months).

1418

1419

1420

1421

1422 **Analysis of RNA-sequencing data**

1423 **RNA-seq data processing and identification of differentially expressed genes**

1424 Single-end RNA-seq samples with 40 base pair (bp) read lengths were mapped to the human

1425 genome (GRCh38) and ERCC spike-in sequences. Reads were mapped to the genome using

1426 Bowtie2 (version 2.3.4.3) and default parameters. Reads that overlapped with the genomic

1427 location for exonic regions were used to calculate gene counts with the FeatureCounts (Subread

1428 package of version 1.6.3) package. Further, spike-in read counts were used for each sample to

1429 normalize the library sizes. These read counts were used to calculate the sample-specific size

1430 factor by using the function estimateSizeFactors (DESeq2) available in R. Normalized sample

1431 coverage profiles were then created from previously determined size factors by using

1432 bamCoverage (DeepTools v3.0.2) and parameters "--scaleFactor --skipNonCoveredRegions". To

1433 check the reproducibility of biological replicates for each condition, principal component analysis

1434 (PCA) and correlation (Spearman's rank coefficient) were assessed from the sample coverage

1435 profiles at genome-wide scale and visualized using scatterplots and heatmaps. Because these

1436 analyses showed a high correlation of sample coverage profiles between replicates, replicates

1437 were merged using samtools merge and processed again as described for the individual

1438 replicates. Next, differential gene expression analysis was performed using the DESeq2 in R. To

1439 detect differentially expressed genes (DEGs) in each sample, raw read counts from RNA-seq

1440 data were imported to the DESeq2 and the size factors calculated using the estimateSizeFactors

1441 function. A transcript with an absolute log2 fold-change ≥ 1.5 and an adjusted *P*-value ≤ 0.01 was

1442 considered significant.

1443

1444 **Enrichment analysis**

1445 Gene ontology enrichment for selected gene sets was performed by the Enrichr program

1446 (https://amp.pharm.mssm.edu/Enrichr/). All GO terms were ranked based on the Enrichr

1447 combined score, calculated by multiplying the adjusted *P*-value with the z-score using the Fisher's

1448   exact test. The Fisher's exact test was used to determine significant overlaps between the queried

1449   gene sets and other publicly available datasets. Enrichment of gene sets was considered

1450   significant for an adjusted P-value ≤ 0.01, unless stated otherwise.

1451

1452   **Estimation of immune cell content in neuroblastoma tumors**

1453   Cell type identification by estimating relative subsets (CIBERSORT) [43], a deconvolution method

1454   was used to evaluate immune cell fractions from gene expression data using the R package

1455   'immunedeconv'. RNA transcript estimations were generated for all 498 neuroblastoma tumors

1456   using the LM22 signature matrix available for 22 immune cell types. CIBERSORT was run in

1457   "Absolute mode" with disabled quantile normalization as recommended for tumor RNA-seq data

1458   and the overall immune content produced by the algorithm compared among tumors.

1459

1460   **ChIP-seq analysis**

1461   **Data processing-** All ChIP-seq raw datasets were processed as previously described [83]. The raw

1462   read quality of the samples was accessed using the Fastqc tool (v0.11.7) to identify possible

1463   sequencing errors and biases. Reads were aligned to the human genome (build hg19,

1464   GRCh37.75) using the mapper Bowtie (v2.3.4.3) with default parameters. Unique and non-

1465   duplicate reads that mapped to the reference genome were further processed using Samtools

1466   (v1.9) and the MarkDuplicates (v2.1.1) command of Picard tools. Next, antibody enrichment in

1467   each replicate as compared to input samples was verified using the PlotFingerprint command of

1468   deepTools (v3.1.1). Peak caller MACS2 (2.1.1) was used to identity narrow peaks (H3K4me3 and

1469   H3K27ac) with the parameters "--q 0.01--call-summits" and broad peaks (H3K27ac and

1470   H3K27me3) with the parameters "--broad-cutoff 0.01". Peaks that overlapped with black-listed

1471   regions (http://mitra.stanford.edu/kundaje/akundaje/release/blacklists/) of the reference genome

1472   (mostly comprised of major satellite repeats of telomeric and pericentromeric regions) were

1473   filtered out. Command "bamCompare" from the deepTools was used with the parameters "--

1474   scaleFactorsMethod readCount --binSize 40 --operation subtract --smoothLength 80 --

1475   extendReads 200" to create the input normalized bedgraph tracks for each replicate and

1476   afterwards negative values were set to zero and counts were scaled to reads per million/base pair

1477   (rpm/bp) to account for differences in the library size. Bigwig files were created for visualization

1478   with bedGraphToBigWig. Subsequently, correlations among the ChIP-seq replicates were

1479   accessed using bigwigs with the command "multiBigwigSummary" from deepTools and highly

1480   correlated replicates merged at the BAM level. Peak identifications were then repeated in the

1481   same manner for these merged BAM files.

1482

1483   **Identification of super-enhancer regions-** Super-enhancers (SEs) were identified using the

1484   ROSE algorithm (https://bitbucket.org/young_computation/rose/src/master/). Briefly, H3K27ac

1485   binding regions identified by MACS2 as significant peaks, termed typical enhancers, were stitched

1486   together if they were within 12.5 kb of each other. These stitched enhancers were ranked by

1487   comparing the H3K27ac signal (density * length) with the input signal. The ROSE algorithm was

1488   used to determine the inclination point for all stitched H3K27ac signals and to segregate regular

1489   enhancers from SEs. To compare SEs in 5Y-parental, 5Y-LDK-resistant and SH-EP cells, the

1490   same maximum threshold was used between the conditions.

1491

1492   **Analysis of histone binding changes between lineage states-** To analyze the changes in

1493   occupancies of active (H3K27ac and H3K4me3) and repressive (H3K27me3) histone marks

1494   during the transition from adrenergic (5Y-par.) to mesenchymal (5Y-LDK-res., SHEP) states, we

1495   compared the peaks of histone marks identified by MACS2 at the promoter regions. For this

1496   purpose, we first extracted the promoter regions ± 2 kb with respect to the TSS (-2kb upstream

1497   to +2kb downstream) of all annotated protein coding genes and subsequently, retrieved the peaks

1498   of H3K27ac, H3K4me3 and H3K27me3 from 5Y-par., 5Y-LDK-res. and SH-EP cells. Now, to

1499   determine the differential binding of each histone mark between 5Y-par. and 5Y-LDK-res. cells,

1500   we first combined all significant peaks called by MACS2 at the promoter regions and merged the

1501   peak regions that overlapped by at least 50%. This 50% threshold was used to avoid merging

1502   peaks that had clear and distinct summits. Next, the normalized active or repressive histone

1503   marks read densities were calculated for each region and a ratio of [log2 (5Y-LDK-res./ 5Y-par.)]

1504   was calculated. Shared peaks had similar enrichment of either active or repressive histone marks

1505   in both the cell types. Similar comparisons were made for active or repressive histone marks

1506   between 5Y-par. and SH-EP cells. To further compare changes in all histone marks at the

1507   promoters of immune genes, the gain of significant H3K27ac, H3K4me3 binding and loss of

1508   H3K27me3 signals were listed in mesenchymal (5Y-LDK-res., SHEP) cells as compared to

1509   adrenergic (5Y-par.) cells.

1510

1511   **Integrated analysis of histone binding and gene expression-** Cell-type specific differential

1512   enrichment of H3K27me3 and H3K4me3 binding in 5Y-par., 5Y-LDK-res. and SH-EP cells was

1513   determined by calculating the log2 (H3K4me3+1/H3K27me3+1) ratios in the promoter regions

1514   (TSS ± 2 kb) of immune genes. Next, to examine the association between gene expression and

1515   differential enrichment of H3K27me3 and H3K4me3 binding in immune genes in 5Y-par., 5Y-LDK-

1516   res. and SH-EP cells, genes were ranked based on their expression values and plotted against

1517   the calculated ratios between the histone marks.